Crystallization Kinetics of Olivine-Phyric Shergottites

A Thesis Presented for the
Master of Science
Degree
The University of Tennessee, Knoxville

Megan Elizabeth Ennis
May 2014

DEDICATION

To Mom and Dad

ABSTRACT

Petrographic and geochemical techniques applied to Martian meteorites can reveal their petrogenesis, and ultimately the magmatic evolution and thermal history of Mars. Two quantitative textural tools, crystal size distribution (CSD) and spatial distribution pattern (SDP) analysis, are utilized to describe the early crystallizing phases, olivine and pyroxene, of one olivine-phyric shergottite (EET 79001A, DaG 476, and Dho 019) from each sampling locality as inferred from Mars ejection ages. Qualitative observations of trace element zonation patterns (P, Cr, and Al) in olivine are used in conjunction with CSD and SDP to characterize the crystallization history of these samples. Previously reported CSDs are re-evaluated using a newer stereographically corrected methodology. The linear CSDs for pyroxene in DaG 476 and EET 79001A indicate single populations that grew under steady-state conditions. The CSDs for olivine in the three meteorites analyzed are more complex. Kinks in the olivine CSD plot for DaG 476 suggest up to three populations crystallized at different cooling rates. The olivines CSD for both EET 79001A and Dho 019 are dominated by single linear trends representing one crystal population; however, elemental X-ray mapping suggests two populations in Dho 019. A variety of P zonation patterns are present in olivine grains in these samples. Oscillatory P zonation suggests variation in growth rate, where high-P olivine experienced rapid growth compared to low-P olivine. Residence times are calculated using CSD slopes and an assumed constant growth rate. As implied by the observed P zonation in olivines, ranges of residence times are presented using different growth rates inferred from previous experimental data. SPD analysis classifies the pyroxene populations in DaG 476 and EET 79001A as clustered touching frameworks,

indicating that the crystals grew or accumulated in clusters rather than as randomly distributed grains. The olivines in DaG 476 and Dho 019 are also clustered but are classified as non-touching frameworks. Quantitative textural analyses, used in conjunction with quantitative elemental mapping, also provide constraints on the origin of the olivine megacrysts in these martian meteorites. The data indicate that most of the olivines are phenocrysts or antecrysts, although small amounts of xenocrysts may also be included.

TABLE OF CONTENTS

CHAPTER I Introduction 1

CHAPTER II Analytical Techniques 4

2.1 Crystal Size Distribution 4

2.2 Spatial Distribution Pattern Analysis 13

2.3 Phosphorus Zonation 14

CHAPTER III Results 17

3.1 Crystal Size Distribution 17

3.2 Spatial Distribution Pattern Analysis 22

3.3 Phosphorous Zonation 23

CHAPTER IV Discussion 28

4.1 Comparison of 2D and 3D CSD Plots 28

4.2 Growth Rates and Residence Times 32

4.3 Spatial Distribution Pattern Analysis 38

4.4 Implications for Shergottite Crystallization 39

4.4.1 DaG 476 39

4.4.2 EET 79001A 44

4.4.3 Dho 019 49

4.5 Origin of Megacrysts 54

CHAPTER V Conclusions 58

LIST OF REFERENCES 61

APPENDIX 69

Appendix A 70

Appendix B 76

Appendix C 82

Vita 99

LIST OF TABLES

Table 1. CSD data* 18

Table 2. Cooling rates and residence times. 34

Table 3. Crystal habits for the five best-fit shape curves for DaG 476 olivine grains..... 77

Table 4. Crystal habits for the five best-fit shape curves for DaG 476 pyroxene grains. 78

Table 5. Crystal habits for the five best-fit shape curves for EET 79001A olivine grains. 79

Table 6. Crystal habits for five best-fit shape curves for EET 79001A pyroxene grains. 80

Table 7. Crystal habits for the five best-fit shape curves for Dho 019 olivine grains. 81

LIST OF FIGURES

Figure 1. (a) Original crystal size distribution plot illustrating the linear relationship between the natural logarithm of the population density and the crystal length (modified after Higgins, 2006). (b) Modifications to the original linear CSD can reflect physical processes within the magma chamber, where annealing creates a turndown at the small size interval, fractionation deflects the original CSD downward at the large size interval (modified after Marsh, 1988), and magma mixing produces a "kinked" CSD such that a slope can be recovered for the population of magma A and magma B (modified after Higgins, 1996). 5

Figure 2. (a) PPL image, (b) XPL image, and (c) BSE image of the portion of DaG 476 used to acquire pyroxene grain traces. (d) BSE image with select pyroxene grains traced. (e) Pyroxene grain traces used in *ImageJ64*. (f) *CSDslice* output comparing the shape curve of the best-fit crystal habit with the shape curve of the measured population. 10

Figure 3. (a) Mg K_β, (b) P K_α, (c) Cr K_α, and (d) Al K_α elemental x-ray maps of EET 79001A olivine grain in groundmass of pyroxene and maskelynite. (Image colors are not directly scaled; warm colors represent higher abundances than cool colors.).... 16

Figure 4. CSD patterns for (a) DaG 476 olivine, (b) DaG 476 pyroxene, (c) EET 79001A olivine, (d) EET 79001A pyroxene, (e) Dho 019 olivine, and (f) SDP analysis. 21

Figure 5. Mg K_β, P K_α, and Cr K_α x-ray maps for Dho 019 olivine grains. (a-c) Olivine 1 contains two P-rich cores surrounded by low P olivine and oscillatory rims with a correlation between P and Cr. (d-f) Olivine 2 exhibit a skeletal pattern in the P zoning with no correlation between Mg and Cr. (g-i) Olivine 3 displays sector

zoning around a high P melt inclusion. (j-l) Olivine 4 (upper grain) contains a P-rich core surrounded by low P olivine, where off sets in the P-rich core shows evidence of microfaulting. (Image colors are not directly scaled; warm colors represent higher abundances than cool colors.) 24

Figure 6. A comparison of residence times calculated for the individual crystal populations in DaG 476, EET 79001A, and Dho 019. 36

Figure 7. DaG 476 olivine megacryst. a) BSE image. b) Mg K_β x-ray map illustrates Mg-rich cores (red). c) P K_α x-ray map with no zonation in core and high-P (green-red) oscillatory bands on rims. The small olivine in the lower left has oscillatory zoning too and is relatively high in P (red-white). d) Cr K_α x-ray map illustrates the chromite rich cores in the olivine (small white grains). e) Crystal size distribution of olivine in DaG 476 with three linear segments representing three olivine populations. (Image colors are not directly scaled; warm colors represent higher abundances than cool colors.) 41

Figure 8. EET 79001A olivine megacryst. a) BSE image. b) Mg K_β x-ray map illustrates Mg-rich core (red). c) P K_α x-ray map with high-P in core, but no well-defined zonation (green-yellow). The small olivine in the upper right is low in P, but has faint sector zoning (bluish white). d) Cr K_α x-ray map illustrates the chromite rich cores in the olivine (small red grains). e) Crystal size distribution of olivine in EET 79001A with two linear segments indicating steady state conditions for much of the cooling history. (Image colors are not directly scaled; warm colors represent higher abundances than cool colors.) 46

Figure 9. Dho 019 olivine megacryst. a) BSE image. b) Mg K_β x-ray map illustrates reverse Mg-Fe zonation with high Mg on right most rim (red). c) P K_α x-ray map where high-P core (green) shows evidence of resorption and oscillatory P-rich bands are present on the rims. d) Cr K_α x-ray map illustrates the chromite rich core in the olivine on the right (small green-red grains). e) Crystal size distribution of olivine in Dho 019 with two linear segments representing two olivine populations. (Image colors are not directly scaled; warm colors represent higher abundances than cool colors.) 51

Figure 10. a) SEM image of DaG 476 thin section used to trace olivine and pyroxene grains. b) Olivine and pyroxene grain traces. 71

Figure 11. a) SEM image of second DaG 476 thin section used to trace olivine grains. b) Olivine grain traces. 72

Figure 12. a) SEM image of EET 79001A thin section used to trace olivine and pyroxene grains. b) Olivine and pyroxene grain traces. 73

Figure 13. a) SEM image of EET 79001A thin section used to trace olivine grains. b) Olivine grain traces. 74

Figure 14. a) SEM image of Dho 019 thin section used to trace olivine grains. b) Olivine grain traces. 75

Figure 15. The five best-fit shape curves output from *CSD Slice* for DaG 476 olivine grains compared to the shape curve for the actual grain population (sa/la = short axis/long axis). 77

Figure 16. The five best-fit shape curves output from *CSD Slice* for DaG 476 pyroxene grains compared to the shape curve for the actual grain population (sa/la = short axis/long axis). 78

Figure 17. The five best-fit shape curves output from *CSD Slice* for EET 79001A olivine grains compared to the shape curve for the actual grain population (sa/la = short axis/long axis). 79

Figure 18. The five best-fit shape curves output from *CSD Slice* for EET 79001A pyroxene grains compared to the shape curve for the actual grain population (sa/la = short axis/long axis). 80

Figure 19. The five best-fit shape curves output from *CSD Slice* for Dho 019 olivine grains compared to the shape curve for the actual grain population (sa/la = short axis/long axis). 81

Figure 20. Elemental x-ray maps for olivine grains in DaG 476 were acquired for each of the areas outlined in red on the SEM image. 83

Figure 21. Al K_α x-ray map of DaG 476 olivine. 84

Figure 22. DaG 476 olivine grain. a) Mg K_β x-ray map. b) P K_α x-ray map. c) Cr K_α x-ray map. d) Al K_α x-ray map. 85

Figure 23. DaG 476 olivine grain. a) Mg K_β x-ray map. b) P K_α x-ray map. c) Cr K_α x-ray map. d) Al K_α x-ray map. 86

Figure 24. DaG 476 olivine grain. a) Mg K_β x-ray map. b) P K_α x-ray map. c) Cr K_α x-ray map. d) Al K_α x-ray map. 87

Figure 25. DaG 476 olivine grain. a) Mg K_β x-ray map. b) P K_α x-ray map. c) Cr K_α x-ray map. d) Al K_α x-ray map. 88

Figure 26. Elemental X-ray maps for olivine grains in EET 79001A were acquired for each of the areas outlined in red on the SEM image. 89

Figure 27. Al K_α x-ray map of EET 79001A olivine. 90

Figure 28. EET 79001A olivine grain. a) Mg K_β x-ray map. b) P K_α x-ray map. c) Cr K_α x-ray map. d) Al K_α x-ray map. 91

Figure 29. Elemental X-ray maps for olivine grains in Dho 019 were acquired for each of the areas outlined in red on the SEM image. 92

Figure 30. Dho 019 olivine grain. a) Mg K_β x-ray map. b) P K_α x-ray map. c) Cr K_α x-ray map. 93

Figure 31. Dho 019 olivine grain. a) Mg K_β x-ray map. b) Fe K_α x-ray map. c) P K_α x-ray map. d) Cr K_α x-ray map. 94

Figure 32. Dho 019 olivine grain. a) Mg K_β x-ray map. b) Fe K_α x-ray map. c) P K_α x-ray map. d) Cr K_α x-ray map. 95

Figure 33. Dho 019 olivine grain. a) Mg K_β x-ray map. b) Fe K_α x-ray map. c) P K_α x-ray map. d) Cr K_α x-ray map. 96

Figure 34. Dho 019 olivine grain. a) Mg K_β x-ray map. b) Fe K_α x-ray map. c) P K_α x-ray map. d) Cr K_α x-ray map. 97

Figure 35. Fe K_α x-ray maps for olivines in a) figure 9, b) figure 5g-i, and c) figure 5j-l. 98

CHAPTER I

INTRODUCTION

Remote sensing of Mars has revealed a plethora of volcanic sites, many of which exhibit multiple flows. Martian meteorites form distinct clusters on a Mars ejection age timeline, as determined from cosmogenic nuclides, suggesting that they may sample up to seven of these volcanic regions (McSween, 2008). Although most olivine-phyric shergottites (Goodrich, 2002) have the same ejection age, representing a single impact event, a few outliers suggest launch in two other impact events from different locations; therefore, the olivine-phyric shergottites may be widely distributed on the Martian surface.

Olivine-phyric shergottites have a distinctive porphyritic texture, with large olivine megacrysts set in a fine-grained basaltic groundmass dominated by pigeonite, augite, and interstitial plagioclase, which has been subsequently converted to maskelynite via shock (Goodrich, 2002; Greshake *et al.*, 2004; Lentz and McSween, 2000; Mikouchi and Miyamoto, 2002; Mikouchi et al., 2001; Taylor *et al*., 2002; Walton *et al.*, 2005). Quantitative textural observations of these igneous samples can provide information about the effects of kinetic and equilibrium processes operating during magmatic crystallization. Three different kinds of textural relationships are explored here.

The crystal size distribution (CSD) of a phase is most often analyzed using a classic CSD plot, where a linear relationship exists between the natural logarithm of the population density and crystal size, such that the intercept and slope can provide estimates of effective nucleation density and residence time in a magma chamber

(Cashman and Marsh, 1988; Marsh, 1988). Modifications from the linear CSD can reflect a variety of geologic processes, such as crystal accumulation or loss during fractional crystallization, magma mixing, and magma ascent (Higgins, 1996; Marsh, 1998). CSDs have been determined for the olivine and pyroxene populations in some olivine-phyric shergottites (Goodrich, 2003; Greshake *et al.*, 2004; Lentz and McSween, 2000; Lentz and McSween, 2005; Taylor *et al.*, 2002; Walton *et al.*, 2005). However, improvements in the methods of data collection and conversion from two-dimensional data to representative three-dimensional CSDs (Higgins, 2000; Morgan and Jerram, 2006) indicate that many of the previously reported CSDs should be reanalyzed. Because of differences in grain size measurement techniques, this requires that data be reacquired.

Textural and compositional relationships observed in many olivine-phyric shergottites suggest disequilibrium between of the olivine megacrysts and the groundmass (Goodrich, 2002, and references therein), leading to some uncertainty in the origin of the olivines. Originally interpreted as xenocrysts (McSween *et al*., 1979), a portion of the megacrysts in some olivine-phyric shergottites has been reinterpreted as phenocrysts by some authors (e.g. Goodrich, 2003 and Zipfel, 2000) and more recently as antecrysts (Balta *et al.*, 2013).

Agglomeration of crystals to form larger clusters (glomerocrysts) is common in igneous samples. The spatial distribution pattern (SDP) can be used to characterize a population of grains as ordered or clustered and to describe their crystal framework as touching or non-touching (Jerram *et al.*, 1996; Jerram *et al.*, 2003). Clustering of olivine has been observed in the olivine-phyric shergottite *Dhofar 019* (Taylor *et al.*, 2002); however, the timing and origin the crystal clustering remains elusive.

Phosphorus zoning in olivine has been observed in terrestrial and extraterrestrial samples (Milman-Barris *et al.*, 2008), with preliminary findings of zonation within several olivine-phyric shergottites reported by Beckett *et al.* (2008). Despite the low elemental abundance of phosphorus in olivine, x-ray intensity maps of its distribution in individual grains and glomerocrysts reveal zonation patterns that may provide insight into the earliest stages of crystallization (Milman-Barris *et al.*, 2008).

One olivine-phyric shergottite was selected from each of three Mars ejection age clusters (0.73 Ma, 1.2 Ma, and 20 Ma; McSween, 2008), which are thought to represent distinct sampling localities, for analysis in this study. These samples are Elephant Moraine (EET) 79001 lithology A, Dar al Gani (DaG) 476, and Dhofar (Dho) 019. The current study re-evaluates olivine and pyroxene populations to obtain stereographically corrected three-dimensional CSDs using the methods of Higgins (2000) and Morgan and Jerram (2006). The results, including CSD shape and slope, are then compared to previous work. The quantitative analysis of the SDP is used in conjunction with the qualitative description of phosphorous zonation to support the interpretations of the CSDs. The implications for the crystallization history of these samples, and therefore past magmatic processes on Mars, are discussed.

CHAPTER II

ANALYTICAL TECHNIQUES

2.1 Crystal Size Distribution

Crystal size distribution (CSD) analysis is a well-established, statistically valid tool used for quantitative textural description of crystalline rocks. The analysis describes crystal size of a population as a function of constant growth rate and residence time (Higgins, 2006; Marsh, 1988). Crystal content as a function of crystal size provides a direct approach to modeling crystallization within magmatic systems, and therefore insight into the dynamics of the system including time variations of nucleation and growth (Marsh, 1988). Extensive descriptions of CSD theory and its application to crystalline samples have been provided by Cashman and Marsh (1988), Marsh (1988), and Marsh (1998).

The population density (n), also referred to as the number density, is the ratio of the number of crystals in a given size interval (dN) to that size interval (dL) for the volume of interest. This value is determined using a cumulative histogram of the number of crystals in defined size ranges (bins). For a steady state system with continuous nucleation and growth, the basic interpretation of a classic CSD plot (Fig. 1a) was described by Marsh (1988) as a linear relationship between the natural logarithm of the population density (n) and crystal size (L). This relationship can be expressed as:

$$\ln(n) = \ln(n_o) - \frac{L}{G\tau} \qquad (1)$$

where n_o is final nucleation density, L is crystal size (length or width), G is growth rate, and τ is residence time. The intercept (at $L = 0$) of the linear regression is the effective nucleation density (n_o) and the slope is the negative inverse of the characteristic length (C), where $C = G\tau$ (Fig. 1a). The characteristic length describes the dominant size within a defined population (Cashman and Marsh, 1988). If either the growth rate (G) or the residence time (τ) is known, the other can be solved for mathematically.

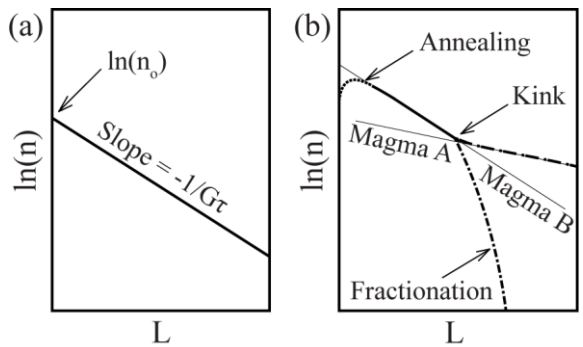

Figure 1. (a) Original crystal size distribution plot illustrating the linear relationship between the natural logarithm of the population density and the crystal length (modified after Higgins, 2006). (b) Modifications to the original linear CSD can reflect physical processes within the magma chamber, where annealing creates a turndown at the small size interval, fractionation deflects the original CSD downward at the large size interval (modified after Marsh, 1988), and magma mixing produces a "kinked" CSD such that a slope can be recovered for the population of magma A and magma B (modified after Higgins, 1996).

Physical processes within the magma chamber can modify the original linear CSD (Fig. 1b), such that inspection of the shape of the CSD will provide insight into magma chamber processes. Fractionation will deflect the CSD downward as the larger size fraction of crystals is removed from the system, whereas crystal accumulation will deflect the original CSD upward as the larger size fraction is increased (Marsh, 1988; Marsh, 1998). A turndown at small size intervals can result from destruction of fine crystals

through annealing or continued growth without further nucleation (Marsh, 1988). A curved concave upward or "kinked" CSD can result from changes in the system due to magma ascent (Armienti *et al*., 1994) or from magma mixing (Fig. 1b; Higgins, 1996). The slopes can be recovered for multiple populations of crystals that result from accumulation, magma ascent, or magma mixing, via the regression of each linear segment of the CSD (Fig. 1b). The Marsh (1988) steady-state model remains applicable; however, magma mixing or accumulation result in lower slope intercepts or nucleation rates (Higgins, 1996).

Direct collection of three-dimensional crystal size data is ideal, but typically impractical or impossible. Therefore, two-dimensional data must be converted and corrected via the principles of stereology to obtain a reliable three-dimensional CSD. Methods have been developed that address many issues related to this conversion (Higgins, 2000; Peterson, 1996; Sahagian and Prooussevitch, 1998). *CSD Corrections v. 1.39* is a program that has been developed to apply the necessary stereographic corrections to two-dimensional length and width data in order to generate a three-dimensional CSD (Higgins, 2000). The program accepts the input of two-dimensional length or width measurements obtained from either a best-fit ellipsoid or box drawn around the grain. Total area measured and calculated percent of the phase are input as well as an estimate of crystal shape, degree of roundness, fabric, quality of fabric, and orientation of section, making the use of this program more rigorous than previous methods.

The estimated crystal shape that is assumed during stereological corrections has a significant influence on the slope of the CSD (Mock and Jerram, 2005). *CSDslice* is a

Microsoft Excel spreadsheet that contains a crystal shape database of 703 different crystal habits (Morgan and Jerram, 2006). Length and width measurements are input, the spreadsheet ratios the crystal measurements (short axis/long axis), and the output is a shape curve based on the frequency of the occurrence of each ratio. The generated shape curve is then compared to the individual shape curve of 703 different crystal habits in the database. The five closest matched shape curves (based on least squares fits), their representative crystal habits, and reliability of fit (R^2) are output. Measurement of 200-250 grains is required for an accurate determination of the crystal habit ($R^2 \geq 0.8$) (Morgan and Jerram, 2006). This number of grains satisfies the proposed minimum number of grains necessary to determine a three-dimensional CSD from two-dimensional data (Mock and Jerram, 2005). *CSDslice* compliments *CSD Corrections v 1.39* as it provides a statistically valid estimate of crystal shape.

The combination of these two programs currently provides the most robust method of attaining a three-dimensional CSD. However, the early methods of Wager (1961) and Kirkpatrick (1977), as described by Marsh (1988), have been utilized to convert two-dimensional data in many published CSDs, including those for the olivine and pyroxene populations in EET 79001A, DaG 476, and Dho 019 (Goodrich, 2003; Lentz and McSween, 2000; Lentz and McSween, 2005; Taylor *et al.*, 2002). The re-evaluation of these CSDs requires the acquisition of new intersection measurements for *CSDslice* input, as only the intersection width or the maximum length was determined in previous work.

Olivine and pyroxene CSDs are determined for olivine-phyric shergottites, as growth of these early crystallizing phases is unimpeded by the late crystallization of

interstitial plagioclase. Effects of impact shock, such as blurred grain boundaries and fractured grains, can make the determination of individual grains and grain boundaries in these meteorites challenging. A variety of section images and x-ray maps were utilized to aid in grain boundary determination. A petrographic microscope was used for the verification of the more ambiguous grain boundaries. The olivine and pyroxene phases can be distinguished from each other and most other phases readily using a BSE image. Whole section x-ray maps are useful in identifying other minor phases. A set of cross polarized light (XPL) images rotated 45° from each other aids in the recognition of grain boundaries when two grains of the same phase are touching, as the extinction of the different grains varies between the two different images. The XPL images are essential for the recognition of the pyroxene grain boundaries, which are more difficult to discern due to the number of contiguous grains. Lentz and McSween (2005) present a CSD for the pyroxene population using the 2D methodology, where only grain widths were measured. However, it was not possible in this study to attain reliable grain traces for the pyroxene population in Dho 019, despite the use of a wide range of images and a petrographic microscope, due to the undulatory and mosaic extinction of the grains resulting from impact shock.

Two thin sections of each sample were used when necessary to obtain an adequate number of grains for an accurate textural analysis (minimum of 200-250; Morgan and Jerram, 2006; Mock and Jerram, 2005), with the exception of EET 79001A where only 75 olivine grains were traced on two thin sections. A petrographic microscope was utilized to collect plane polarized light (PPL; Fig. 2a) and reflected light images of each section, as well as two sets of cross polarized light images (Fig. 2b), rotated

approximately 45° from each other. High-resolution backscatter electron (BSE; Fig. 2c) images were collected on the LEO 1525 field emission scanning electron microscope at the University of Tennessee with an accelerating voltage of ~20 KeV and a magnification of 100x for DaG 476 sections and 250x for EET 79001A and Dho 019 sections. The Cameca SX-100 electron microprobe (EMP) at the University of Tennessee was used to collect whole section x-ray maps with a beam current of 20 nA. Fe, Ca, Al, and Si K_{α} maps were collected with an 8 μm step size for both EET 79001A sections, while for the Dho 019 section, a 2 μm step size was used and a Mg K_{α} map was collected rather than a Si K_{α} map.

Figure 2. (a) PPL image, (b) XPL image, and (c) BSE image of the portion of DaG 476 used to acquire pyroxene grain traces. (d) BSE image with select pyroxene grains traced. (e) Pyroxene grain traces used in *ImageJ64*. (f) *CSDslice* output comparing the shape curve of the best-fit crystal habit with the shape curve of the measured population.

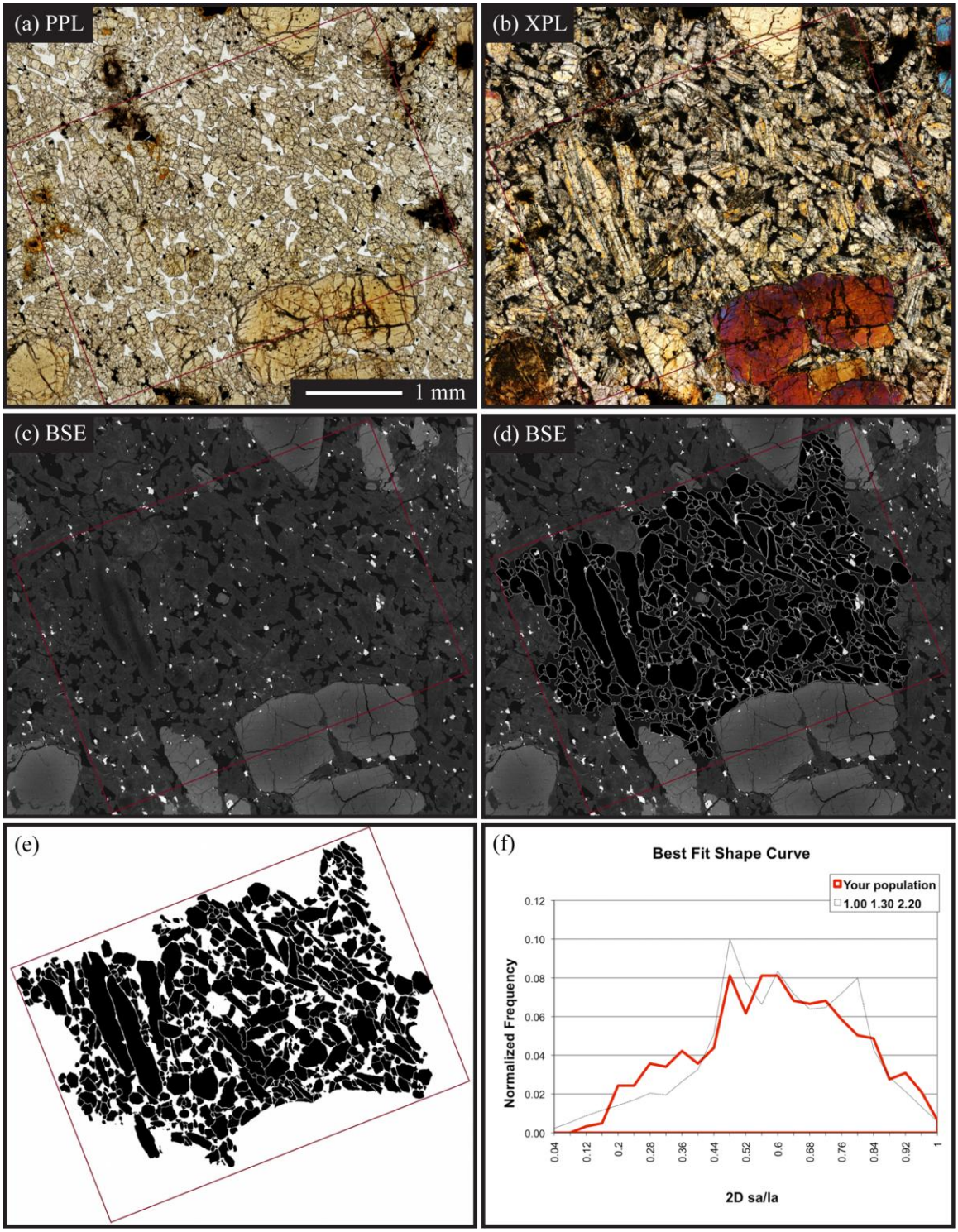

Figure 2. Continued.

Images were stitched together and overlain in *Adobe Photoshop*. The *Adobe Photoshop* auto merge tool can distort the final thin section image; therefore all images were stitched and overlain by hand. Grain boundaries were hand-traced onto the BSE image (Fig. 2d) in *Adobe Illustrator*, as the BSE image provides the most accurate intersection of the grain with the cut surface. The grain boundary traces were exported from *Adobe Illustrator* (Fig. 2e). *ImageJ64* was utilized to determine the length of the long and short axis of a best-fit ellipsoid for each grain boundary trace, as well as the overall degree of roundness of the grains, the number of grain measured, and the total area of the phase traced. The length measurements of the long and short axis were then input into *CSDslice* to get an accurate estimate of the three-dimensional shape of the crystal population (Figure 2f). Finally, the long and short axis length measurements, total area of the phase measured, total area measured, degree of roundness, and determined crystal habit were input into *CSD Corrections v. 1.39*, along with estimates of the fabric , quality of fabric, and orientation of section (Higgins, 2000). This program calculated the three-dimensional CSD from the measured two-dimensional data and output the corresponding CSD plot.

2.2 Spatial Distribution Pattern Analysis

The spatial distribution pattern (SDP) is a quantifiable, textural descriptor that is used to characterize the packing arrangement and distribution of grains. The SDP of grains in two dimensions can be described using a value of R, which is defined as the ratio of the mean nearest neighbor distance of the phase ($\Sigma r/N$) to the predicted mean nearest neighbor distance for a random distribution of points ($1/2\sqrt{\rho}$). Therefore, the R-value can be expressed as:

$$R = \frac{2\sqrt{\rho}\sum r}{N} \qquad (2)$$

where ρ is the density of the population, r is the nearest neighbor distance, and N is the total number of grains measured (Jerram *et al.*, 1996). In a random distribution of grains R = 1, while R > 1 and R < 1 reflect ordering and clustering, respectively (Clark and Evans, 1954). Jerram *et al.* (1996) proposed a reference texture of randomly packed spheres of equal size for the determination of the SDP in three dimensions; however, the SDP of these spheres varies with porosity (% melt or other phases). Modeled variations in R with respect to porosity produce a random sphere distribution line (RSDL) on a plot of porosity versus R, where values of R that plot above the line are consider to be ordered while those below the line are clustered (Jerram *et al.*, 1996). Clustered or ordered populations can also be classified as a touching or non-touching crystal framework according to the value of R (Jerram *et al.*, 2003), which has implications for the history of formation of the texture. Taylor *et al.* (2002) reported clustering in the olivine population of Dho 019. Analysis of the SDP for the olivine-phyric shergottites will aid in the quantification of the grain populations and interpretation of crystallization histories.

The R-values were determined using *Big-R* software (now available in *CSD Corrections v. 1.40*) for the olivine and pyroxene populations in each sample, with the exception of the olivine population of EET 79001A. This program requires the input of the XY grain center coordinates and total area of the phase measured. These data were acquired using *ImageJ64*, where the center of the best-fit ellipsoids of the grain traces were output with the total area measured.

2.3 Phosphorus Zonation

Phosphorus zonation patterns have been observed, and are believed to be common, in the olivine grains of terrestrial volcanic rocks (basalts, komatiites, andesites, and dacites) and extraterrestrial samples (Martian meteorites, ordinary chondrites, and lunar rocks) (Beckett *et al.*, 2008; McCanta *et al.*, 2008, 2009; Milam-Barris *et al.*, 2008). X-ray intensity maps of igneous olivine grains have yielded a variety of phosphorus zoning patterns, which are often positively correlated, especially in experimental olivines or more equilibrated samples, with the distribution patterns of Cr and, to a lesser degree, Al (McCanta *et al.*, 2009; Milam-Barris *et al*, 2008).

Phosphorus concentrations in olivine can vary from below detectable limits to 0.2-0.4 wt. % over a few microns, with no apparent correlation to Fo content, where the distribution of cations in the crystal reflect their relative distribution coefficients, $D_{Mg, Fe} > D_{Al} > D_{Cr} > D_P$ (Milam-Barris *et al.*, 2008). Beckett *et al.* (2008) presented preliminary results for observed P and Cr zonations in select olivine-phyric shergottites (DaG 489, EET 79001A, and Y-980459). Observations of the preserved phosphorus zonation patterns in olivine-phyric shergottites divulge information about the earliest growth

processes and crystallizing history of the magma that is otherwise unattainable, especially in more equilibrated samples where original Mg-Fe zonation has been disturbed as a result of long residence times at high temperatures. The processes reflected in the P zonation aid in the interpretation of the CSD and SDP results.

A Cameca SX-100 electron microprobe with four spectrometers at the University of Tennessee was used to produce elemental x-ray maps of select olivine grains within one thin section of each shergottite. Three of the four spectrometers were used to acquire qualitative Mg K_β, P K_α, and Cr K_α x-ray maps for each selected olivine grain, while the element for the fourth spectrometer varied between Al K_α, P K_α (using a different crystal), and Fe K_α. No correlations were observed between P and Cr with Al (Fig. 3); therefore, the acquisition of Al x-ray maps was limited and Al maps are not presented further. Due to the low concentration of phosphorus within the olivine grains, maps were produced using a beam current of 200 nA and dwell times of 900 ms at 15 KeV with a step size of 1-3 μm. The images were processed using *ImageJ64* software to apply a look-up table (LUT) and to adjust the brightness and contrast to allow for optimum viewing of the zonation. Due to these adjustments, the color scale is not consistent between images; however, warm colors indicate higher abundances than cool colors. An assortment of representative olivine grains was selected from each of the samples used for CSD analyses based upon their composition and textural relationships.

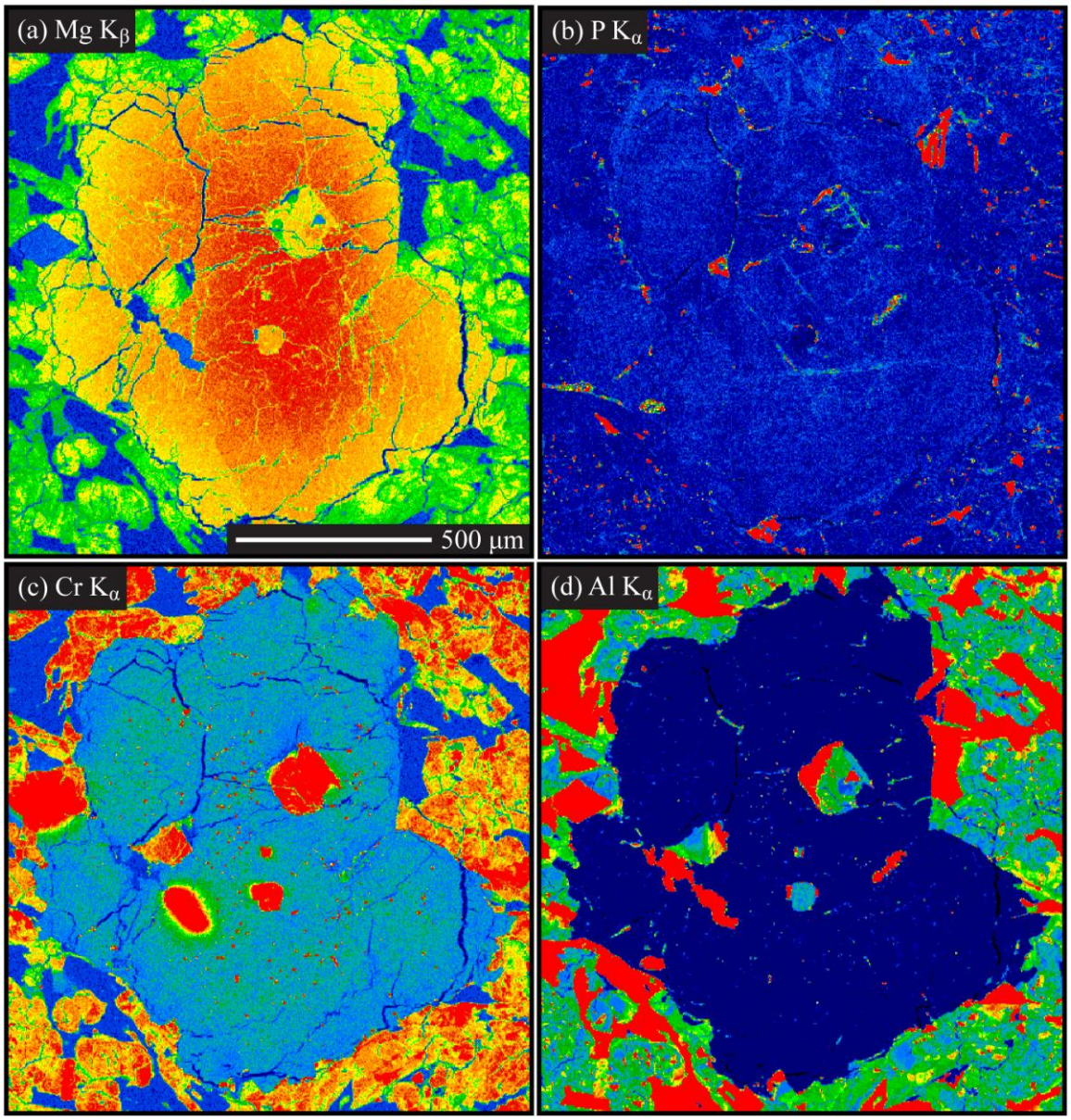

Figure 3. (a) Mg K_β, (b) P K_α, (c) Cr K_α, and (d) Al K_α elemental x-ray maps of EET 79001A olivine grain in groundmass of pyroxene and maskelynite. (Image colors are not directly scaled; warm colors represent higher abundances than cool colors.)

CHAPTER III

RESULTS

3.1 Crystal Size Distribution

Crystal size distribution data and R values from the spatial distribution pattern analysis are presented in Table 1. An adequate number of grains for textural analysis (a minimum of 200-250) were measured for each phase of interest, with the exception of olivine in EET 79001A, where measurements were obtained for only 75 olivine grains (Table 1) using two thin sections. Therefore, higher error is associated with the textural data for this phase in EET 79001A and an accurate R value for the SDP analysis could not be determined. Each predicted crystal habit determined by *CSDslice* met or exceeded the minimum R^2 value of 0.8, indicating a good fit of the frequency of 2D length-width ratios to the predicted shape curve (Morgan and Jerram, 2006) for the olivine and pyroxene populations in each sample, except the olivine in EET 79001A which had an R^2 value of 0.68 for the 75 measured grains. Representative grain aspect ratios utilized in the CSD correction for olivine were 1.00:1.15:1.80 (DaG 476), 1.00:1.40:2.50 (EETA 79001A), and 1.00:1.50:1.90 (Dho 019), respectively. For the pyroxene populations analyzed in DaG 476 and EET 79001A, predicted grain aspect ratios were 1.00:1.25:2.20 and 1.00:1.40:2.10, respectively. Olivine and pyroxene crystal habit predictions have not been used for corrections in previous CSD work on these meteorites.

Table 1. CSD data*

Meteorite	No. of Grains	Area (mm^2)	R value	Shape	Measurement	Avg. Size (mm)	± 1 SD (mm)	Bin Interval	Slope (mm^{-1})	Intercept	R^2	C (mm)
DaG 476												
Olivine	265	164.3	0.78	1.00:1.15:1.80	Length	0.28	0.33	0.79-3.15	-1.83	0.70	0.49	0.55
			0.91					0.079-0.79	-6.21	3.99	0.99	0.16
								0.0125-0.079	-32.70	6.32	0.57	0.03
					Width	0.17	0.21	0.57-2.29	-2.56	1.61	0.78	0.39
								0.091-0.57	-8.07	4.63	0.49	0.12
								0.023-0.091	-36.80	6.89	0.72	0.03
Pyroxene	614	9.2	1.17	1.00:1.25:2.20	Length	0.13	0.12	0.089-0.89	-8.65	8.78	$5x10^{-4}$	0.12
					Width	0.06	0.04	0.11-0.70	-14.60	10.23	0.14	0.07
EET-A												
Olivine	75	97.4	-	1.00:1.40:2.50	Length	0.30	0.40	0.36-3.60	-1.68	0.20	0.78	0.60
								0.036-0.36	-15.50	4.95	0.97	0.06
					Width	0.17	0.25	0.20-3.18	-2.12	1.39	0.79	0.47
								0.032-0.20	-40.40	7.64	0.95	0.02
Pyroxene	418	7.5	1.31	1.00:1.40:2.10	Length	0.15	0.12	0.12-0.76	-9.44	8.77	0.67	0.11
					Width	0.08	0.05	0.11-0.67	-12.00	9.68	0.30	0.08
Dho 019												
Olivine	384	136.5	0.76	1.00:1.50:1.90	Length	0.23	0.17	0.10-1.61	-5.68	4.53	0.25	0.18
								0.016-0.10	-27.10	6.39	0.68	0.04
					Width	0.13	0.10	0.096-0.96	-6.25	5.12	0.07	0.16
								0.015-0.096	-35.60	7.38	0.40	0.03

*Input values for *CSD Corrections 1.39* are as follows: roundness given by *ImageJ 64* is 0.6 for all samples except EET 79001A which is 0.5, fabric is massive, bin setting is 5 bins/decade.

Average grain size (Table 1) was calculated using the length and width data of a best-fit ellipsoid determined by *ImageJ64*. The average size of olivine measured in DaG 476 and EET 79001A are similar (0.28 x 0.17 mm and 0.30 x 0.17 mm, respectively) and slightly coarser than olivine grains measured in Dho 019 (0.23 x 0.13 mm). The average size of pyroxene grains measured in EET 79001A (0.15 x 0.08 mm) is larger than that determined for DaG 476 (0.13 x 0.06 mm). This observation and these measurements are consistent, within error, with pyroxene width measurements reported by Lentz and McSween (2000) for EET 79001A (0.128 mm) and DaG 476 (0.082 mm). The minor differences in reported average grain size may be the result of the analysis of different thin sections.

Slope and intercept data (Table 1) were obtained using *CSD Corrections v. 1.39* (Higgins, 2000), which fits a linear regression that is weighted for the error in each point when individual intersection data are available and error bars have been calculated for each bin interval, as is the case in this study. Greater errors are typically associated with larger size intervals due to the low number of grains in each interval, and with smaller size intervals because the applied corrections are more significant at small grain sizes (Higgins, 2000). A goodness of fit over 0.1 indicates an acceptable fit of the linear regression as determined by the program. The slope at the smallest grain sizes (bin interval 0.096-0.96 mm) for the width measurements for the olivine population in Dho 019 had a low goodness of fit at 0.07. However, the slope and intercept is similar to that determined for the length measurements at that same interval, indicating that the fit is reasonable. The goodness of fit for the slope for the length measurements of the pyroxene population in DaG 476 was very poor (5.0×10^{-4}) and graphically the length

and width measurements present different slopes. This may be the result of a low number of grains in the larger grain size bins.

Slopes can be regressed at three different size intervals using the classic CSD plot (natural log of the population density verses crystal size) for olivine in DaG 476 (Table 1; Figure 4a). The average slope becomes progressively steeper from -2.20 to -7.14 to -34.75 as the grain size decreases. These different slopes may represent different crystal populations, distinct stages in the crystallization history, or some combination of both. Two different linear regressions can be fit to the olivine CSD data for both EET 79001A and Dho 019 (Table 1; Figures 4c,e), which may indicate changes in crystallization or two crystal populations. The slope determined for olivine in EET 79001A at the larger size interval for length and width measurements is slightly steeper (average -1.90), but similar to the previously reported slope of -1.35 for length measurements over a bin interval of 0.9-1.9 mm (Goodrich, 2003). In contrast to the sharp drop in population density of crystals < 1 mm reported by Goodrich (2003), a linear regression with a steep average slope of -27.95 can be fit to the data at the smallest grain size interval. Taylor et al. (2002) reported a slope of -21.7 over a bin interval of 0.1-0.55 mm for width measurements of olivine in Dho 019, which is much steeper than the average slope of -5.97 determined over a larger bin interval that incorporates the previously described width interval. No data at the small grain size interval was previously reported for Dho 019, where a second steeper linear regression, with an average slope of -31.35, can be fit to the data.

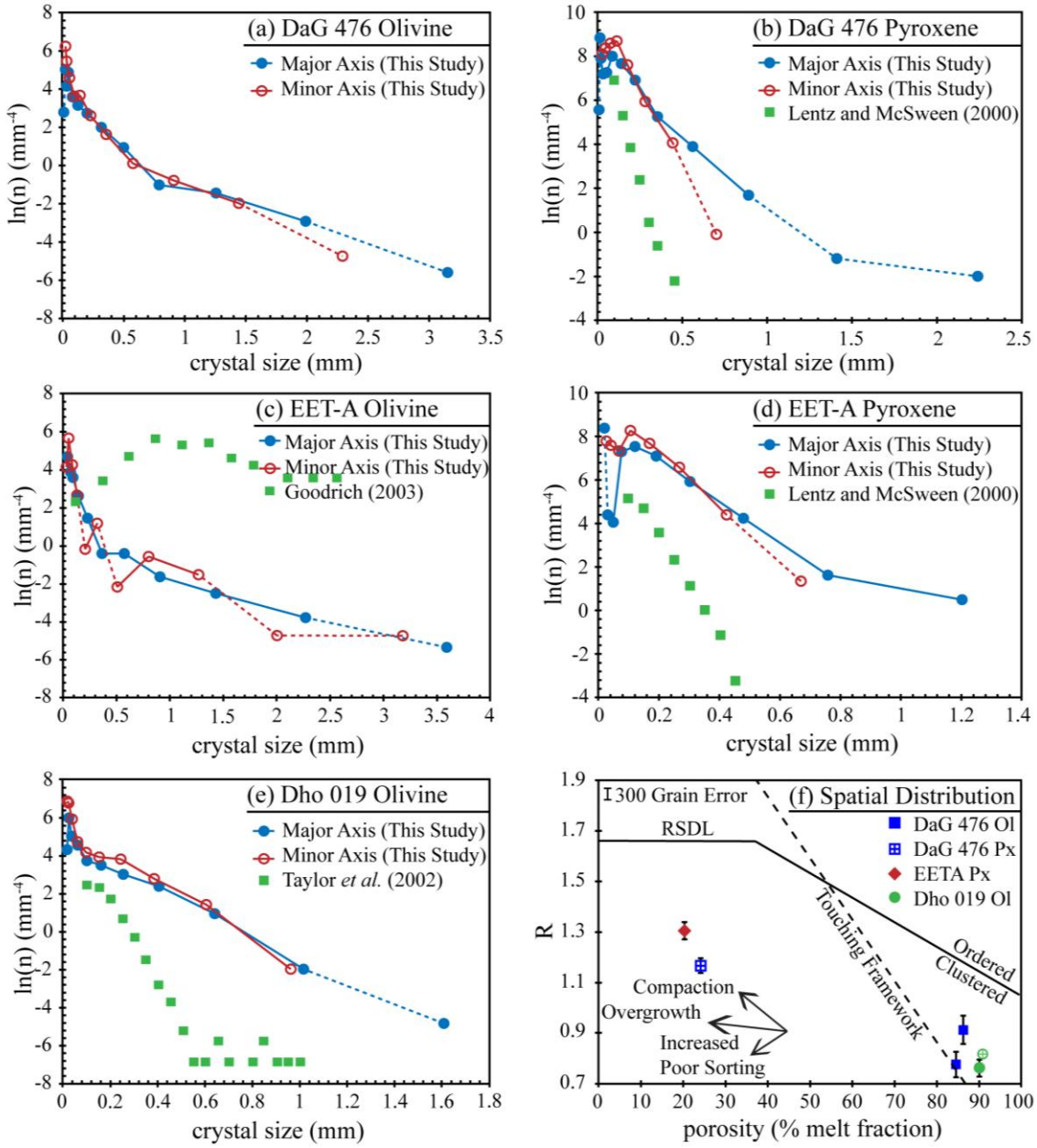

Figure 4. CSD patterns for (a) DaG 476 olivine, (b) DaG 476 pyroxene, (c) EET 79001A olivine, (d) EET 79001A pyroxene, (e) Dho 019 olivine, and (f) SDP analysis.

The CSD plots for the pyroxene population in Dag 476 and EET 79001A both exhibit a single linear trend, suggesting a single stage of crystallization under steady-state conditions of continuous nucleation and growth, with a turndown at the smaller size

fraction indicating possible annealing or continued crystal growth without further nucleation at higher degrees of crystallization (Figures 4b, d). This is consistent with the shape of the CSD reported by Lentz and McSween (2000) for width measurements. However, the stereographically corrected CSD yields an average slope of -11.62 for DaG 476 and -10.72 for EET 79001A, which is shallower than the previously reported slopes of -30.84 (0.10-0.35 mm bin interval) and -24.14 (0.10-0.45 mm bin interval), respectively. The shallower slopes result in an increase in the characteristic length from 0.032 mm to 0.07 mm for DaG 476 and from 0.041 mm to 0.08 mm for EET 79001A. While the shallower slopes yield higher characteristic lengths, the intercepts are very similar, with this study reporting average intercepts of 9.50 mm^{-1} (DaG 476) and 9.23 mm^{-1} (EET 79001A) and Lentz and McSween (2000) reporting 9.92 mm^{-1} and 8.36 mm^{-1} respectively.

3.2 Spatial Distribution Pattern Analysis

R values (Table 1) are plotted relative to the porosity of the sample, or in the case of igneous samples, the percentage of the melt at the time of crystallization, in the graphical representation of the spatial distribution pattern analysis presented in Figure 4f. The percent of melt fraction is best estimated based on the modal abundance of the phase with respect to its relative position in the crystallization sequence: for these meteorites, olivine crystallizes before or simultaneously with pyroxene. The error for each data point was estimated based on the number of grains used for the analysis, as the variation in error increases below a measured sample size of 300 grains (Jerram *et al.*, 1996). Two R values are reported for DaG 476 because two thin sections were used to attain enough

olivine grains for the textural analysis. No R value was obtained for EET 79001A olivine, despite the use of two thin sections, due to the small number of olivine grains present in each thin section. R values for DaG 476 and Dho 019 olivine fall within the clustered, non-touching framework section of the plot (Figure 4f). This observation of Dho 019 olivine is consistent with the previously reported SDP analysis of Taylor *et al.* (2002) (Figure 4f) and is a common feature in phenocryst populations (Jerram *et al.*, 2003). The pyroxene populations of DaG 476 and EET 79001A have lower melt fractions resulting from later crystallization and plot within the clustered, touching framework (Figure 4f).

3.3 Phosphorous Zonation

Observations of element zonation are consistent with those described by Milam-Barris *et al.* (2008), including P-rich melt inclusions surrounded by regions of low-P olivine, oscillatory zoning with possible microfaulting, and P-rich olivine cores that may exhibit skeletal, hopper, or euhedral shapes often surrounded by low-P olivine. Due to the many variations in element zoning patterns that can be observed in a single sample, mapping was completed on five olivines in DaG 476, three olivines in EET 79001A, and ten olivines in Dho 019. X-ray intensity maps of olivine grains within Dho 019 have yielded the greatest variety of phosphorus zoning patterns with complex relationships to other minor cations. This variation is illustrated in Figure 5 with Mg, P, and Cr maps of four select Dho 019 olivine grains whose types of element patterns encompass those observed in DaG 476 and EET 79001A.

Figure 5. Mg K_β, P K_α, and Cr K_α x-ray maps for Dho 019 olivine grains. (a-c) Olivine 1 contains two P-rich cores surrounded by low P olivine and oscillatory rims with a correlation between P and Cr. (d-f) Olivine 2 exhibit a skeletal pattern in the P zoning with no correlation between Mg and Cr. (g-i) Olivine 3 displays sector zoning around a high P melt inclusion. (j-l) Olivine 4 (upper grain) contains a P-rich core surrounded by low P olivine, where off sets in the P-rich core shows evidence of microfaulting. (Image colors are not directly scaled; warm colors represent higher abundances than cool colors.)

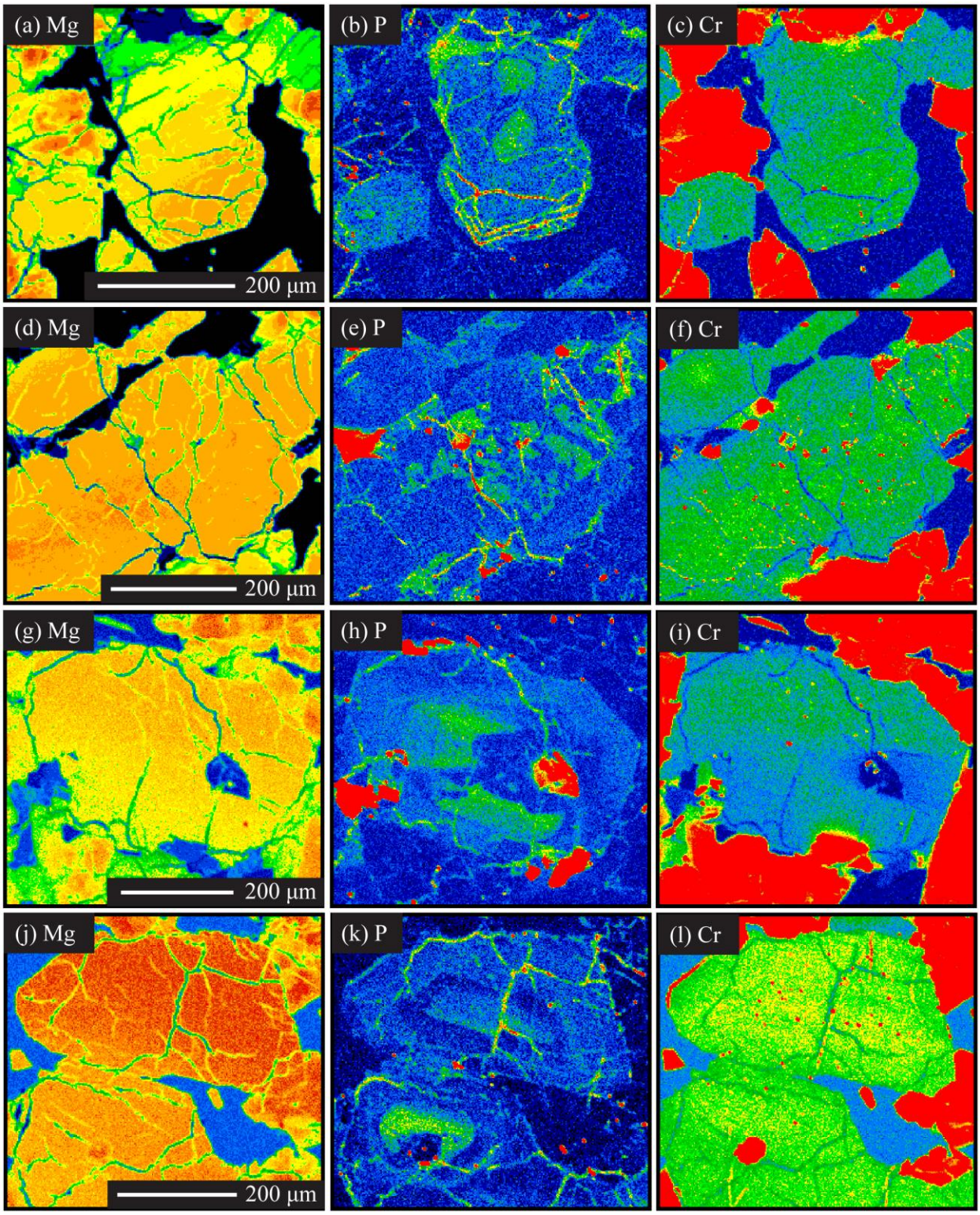

Figure 5. Continued.

No correlation is evident between Fo content (left column of Figure 5) and P zonation (middle column of Figure 5) in any mapped olivine grains. This observation is consistent with previous work, which also recognizes a positive correlation of P zonation with Cr and to a lesser degree Al, especially in experimental olivines or more equilibrated samples (Beckett *et al.*, 2008; McCanta *et al.*, 2008, 2009; Milam-Barris *et al.*, 2008). A few mapped grains exhibit a strong correlation between P and Cr (top row of Figure 5, along the rim of olivine 1), while in most grains this correlation is weak and Cr is more dispersed (third row of Figure 5, olivine 3). No correlation was observed between P and Al in any mapped olivine; therefore the only Al map shown is of EET 79001A (Figure 3d). The homogenization of Fe/Mg and general lack of correlation between P and Cr or Al suggests long residence times at high temperatures (Milam-Barris *et al.*, 2008).

The olivine 1 megacryst (top row of Figure 5) contains two high-P regions within the core (Figure 5b), with no apparent correlation to Fo content or Cr (Figures 5a, c). During an initial period of undercooling, a delay in nucleation may have occurred, which would promote a period of rapid olivine growth necessary to create the high-P cores (Milam-Barris *et al.*, 2008). These high-P cores, which show evidence of resorption, may then have acted as nucleation points for subsequent slower olivine growth (represented by the surrounding low-P region) as the grains grew together, forming a glomerocryst. The rim of this olivine grain contains two high-P bands (Figure 5b) that are positively correlated with Cr (Figure 5c), suggesting rapid olivine growth and shorter residence time for the olivine of the rim compared to that of the core where no P-Cr correlation is observed.

The olivine 2 megacryst (second row of Figure 4) exhibits a completely different zoning pattern in which high-P regions, with no direct correlation to high-Cr regions, produce an overall skeletal pattern. This skeletal region is indicative of rapid olivine growth, which promotes "solute trapping", thus suggesting that the P-enriched olivine is not in equilibrium with the melt (Milam-Barris *et al.*, 2008). The observation of abundant melt inclusions within the high-P skeletal portion of the grain also supports rapid olivine crystallization. Slight Cr zonation is present in the grain (Figure 5f), where the core of the olivine contains higher amounts of Cr than the rim of the olivine.

Sector zoning of P within olivine 3 (Figure 5h) terminates at a low-P region in the olivine adjacent to a large P-rich melt inclusion, consistent with zonation patterns observed by Milam-Barris *et al.* (2008). There is no direct correlation between P and Cr zoning patterns (Figure 5i); however, high Cr regions show a possible correlation with Mg content (Figure 5g), with the exception of the olivine surrounding the melt inclusion that is relatively depleted in Cr.

Olivine 4 has a high-P core surrounded by a region of low P olivine that was subsequently enclosed by high P olivine (Figure 5k). Possible shock deformation features, not visible in the Mg or Cr maps (Figure 5j, l), are observed as minor offsets in the P zoning pattern. High-P observed in fractures may be an artifact of the epoxy used on the thin section or the result of secondary alteration within the fractures.

CHAPTER IV

DISCUSSION

4.1 Comparison of 2D and 3D CSD Plots

Previous CSD measurements using the 2D methodology have been published for olivine and pyroxene in all three meteorites, with the exception of olivine in DaG 476 (Goodrich, 2003; Lentz and McSween, 2000; Taylor *et al.,* 2002). Comparisons with the results of this study are summarized in Figure 4. Overall, the shapes of the plots are similar, but the reported slopes are consistently different. The linear regressions in this study cover larger bin intervals and produce shallower slopes with similar intercepts, with the exception of EET 79001A olivine, where the stereographically corrected CSD gives a slightly steeper negative slope.

The stereographically corrected CSDs for olivine in EET 79001A and Dho 019 (Figure 4c, e) show a slight difference in shape when compared to the previously reported two-dimensional CSD (Goodrich, 2003; Taylor *et al.*, 2002), with a similar slope for EET 79001A. In the previous analyses, a linear segment dominates the CSD plot, with a turndown at smaller crystal sizes and a horizontal leveling at the larger size fraction (Figure 4c,e). The linear portion of the CSD plot suggested continuous nucleation and growth over the bin interval of 0.9-1.9 mm (slope of -1.35) for EET 79001A length measurements (Goodrich, 2003) and over the bin interval of approximately 0.1-0.55 mm (slope of -21.7) for Dho 019 width measurements (Taylor *et al.*, 2002). A large drop in population density in the three smallest size bins was reported for EET 79001A as possibly reflecting a drop in nucleation rate with continued crystal growth during the last

stages of crystallization, and the horizontal leveling of the CSD at the larger size fraction suggested the addition of phenocrysts or xenocrysts (Goodrich, 2003). In Dho 019, minor annealing was proposed for the observed small turnover at the smallest crystal sizes and, similar to EET 79001A, it was suggested that olivine accumulation produced the horizontal leveling at larger crystal sizes (Taylor *et al*., 2002).

The previously reported deviations from the linear CSDs at the smaller and larger crystal sizes are not observed in the corrected CSDs. Rather, a significant "kink" joins two linear segments, with a steep negative slope at smaller crystal sizes and a shallower negative slope at larger crystal sizes (Figure 4c, e). The average slope observed in corrected CSD for EET 79001A olivine at the large size fraction is slightly steeper (-1.90) than the previously reported slope (-1.35). The regression covers a larger range of bin intervals, incorporating all but the smallest bin size in the previously reported data set (Goodrich, 2003), and suggests that the olivine population in EET 79001A grew under a steady-state condition throughout most of its solidification history. The steep negative slope at the smallest size fraction indicates a change in crystallization, perhaps associated with eruption; however, textural examination suggests otherwise (see section 4.4.2).

The horizontal leveling at the larger olivine crystal sizes in Dho 019 (Taylor *et al.*, 2002) is not pronounced in this study, which is consistent with the different 2D and 3D CSDs for olivine in EET 79001A. In the corrected CSD for Dho 019 olivine, all of the previously reported data, including the largest crystal sizes, are incorporated in the linear regression of the larger crystal size population that grew under steady-state conditions. However, the new slope is much shallower (average slope -5.97) than the previously reported slope of -21.7 for width measurements covering a bin interval of 0.1-0.55 mm

(Taylor *et al.*, 2002). The previous study did not report width data for bins smaller than 0.1 mm; therefore, the steep negative average slope of -31.4 that is present at the smallest crystal sizes in the stereographically corrected CSD, was not observed by Taylor *et al.* (2002).

Similar to the previously reported CSDs for pyroxene in DaG 476 and EET 79001A (Lentz and McSween, 2000), the stereographically corrected CSDs for each sample exhibit a single linear trend. Turndowns are observed at small crystal sizes in the corrected CSDs that were not present in the previously reported CSDs as no crystals were measured at the smaller crystal size intervals. The corrected CSDs produce slopes that are shallower than previously reported and cover a larger range of bins. Lentz and McSween (2000) reported a slope of -30.8 for measured widths covering a bin interval of 0.10-0.35 mm for DaG 476 and -24.1 over the bin interval of 0.10-0.45 mm for EET 79001A. The corrected CSD yields an average slope of -11.6 for DaG 476 (bin interval includes lengths 0.089-0.89 mm and widths 0.11-0.70 mm) and -10.7 for EET 79001A (bin interval includes lengths 0.12-0.76 mm and widths 0.11-0.67 mm). Based on the relationship slope = $-1/G\tau$, when growth rate (G) is constant the shallower slopes will result in a shorter residence time (τ).

The CSD data presented are in agreement with the suggestion by Higgins (2000) that population densities can vary greatly when comparing CSD data obtained using outdated methodology to that obtained using the corrected methodology. Typically, the greatest error associated with the methodology of Cashman and Marsh (1988) is reflected in the intercept of the linear regression, not in the value of the slope (Higgins, 2006). For the conversion of two-dimensional thin section data to representative volume data,

Cashman and Marsh (1988) use the equation $n_V(L_{XY}) = n_A(l_{XY})^{1.5}$ (Wager, 1961), where $n_A(l_{XY})$ is the number of intersections per unit area in the interval of l_X to l_Y and $n_V(L_{XY})$ is the number of crystals per unit volume in the interval of L_X to L_Y. Goodrich (2003) used the methodology of Cashman and Marsh (1988), including Wager's conversion equation. The slope of the previously reported CSD (-1.35) is similar to the average slope (-1.90) obtained in this study, but the intercepts are very different. The intercept estimated from the Goodrich (2003) data is ~6.9 and the average intercept determined in this study is 0.80. Although Lentz and McSween (2000) and Taylor *et al.* (2002) reported that the methods of Marsh (1988) and Cashman and Marsh (1988) were used, they do not specify whether or not the conversion equation was applied. A comparison of the previously published data with that of this study reveals very similar intercepts but slopes in this study that are consistently shallower than previously reported.

Higgins (2006) noted that the abundance of crystals at small grain sizes is much less accurate than that of larger crystals, due to the number of corrections applied. This was observed in the current study as well. However, the largest discrepancy in the two data sets may be due to the lack of data at the smallest size intervals in previous studies. Although not specified in the previous studies, differences observed at the smaller size fraction may be attributed to measurement techniques rather than the lack of smaller grain sizes. All tracing for this study was done on high resolution BSE images using x-ray maps and a petrographic microscope to distinguish grain boundaries; previous studies used a variety of images with various resolutions to trace grains, including combined elemental x-ray maps (Ca, Fe, and Al) for olivine in EET 79001A (Goodrich, 2003), Fe and Mg distribution maps for the olivine in Dho 019 (Taylor *et al.*, 2002), and Mg

distribution maps for pyroxene in DaG 476 and EET 79001A (Lentz and McSween, 2000).

Another difference observed between the previously reported CSDs and those in this study is the presentation of the CSD plot. Equal-sized bins were used in the previous studies, whereas logarithmic-sized bins are used in this study. Higgins (2006) showed that plotting the same grain population using logarithmic-sized bins reveals different aspects of the CSD. Fixed width bins tend to conceal information at smaller grain sizes and allow for empty bins (or a fewer number of grains within bins) at the larger size fraction. The use of logarithmic-sized bins allows for an increase in the number of grains in the bins at the larger size fraction. This difference in presentation may account for the loss of the horizontal leveling observed for bin intervals at larger grain sizes in previously published CSDs (Goodrich, 2003; Lentz and McSween, 2000; Taylor *et al.*, 2002).

4.2 Growth Rates and Residence Times

Residence time or growth rate information can be obtained from the slope of the classic CSD plot (Figure 1a) using the equation $m = -1/G\tau$, where m is the slope, G is the growth rate, and τ is the residence time (Higgins, 2006). Unfortunately, experimental growth rate data for shergottites is mostly non-existent. McCoy and Lofgren (1999) conducted cooling rate experiments using a Zagami-like melt composition. The slope of the CSD, created through the analysis of the experimental samples, allowed pyroxene growth rates (average 5.04×10^{-8} mm/s) to be estimated using the growth time based on the experimental cooling rate and temperature interval (Lentz and McSween, 2000). Although there is a lack of experimentally derived growth rates for common silicate

minerals, Marsh (1988) predicts that many silicates might have broadly similar growth rates (~10^{-9} mm/s) based on CSD analysis of samples where residence time can be determined with some accuracy, such as those from lava lakes.

Residence times were estimated for the olivine and pyroxene populations in DaG 476 and EET 79001A and the olivine populations in Dho 019 (Table 2; Figure 6) using the average slope (length and width data) of the respective CSD. To calculate residence time, an average growth rate was calculated using published cooling rate estimates based on olivine Mg-Fe diffusion profiles for DaG 476 and EET 79001A (Mikouchi *et al*., 2001) and Dho 019 (Mikouchi and Miyamoto, 2002). Upper and lower limits are presented for each sample, where the upper limit represents the fastest cooling rate estimate that will produce the observed zonation and the lower limit is the slowest cooling rate estimate required to preserve the zonation. The method of applying independently derived cooling rates to obtain growth rates has been used in previous terrestrial (Jerram *et al.*, 2003) and lunar (Day and Taylor, 2007) CSD studies.

Table 2. Cooling rates and residence times.

		Upper Limit				Lower Limit				Constant Growth Rate	
Meteorite	Grain Size Range	Growth Time (hr)	Avg. Growth Rate (mm/s)	Residence Time (s)	Residence Time (days)	Growth Time (hr)	Avg. Growth Rate (mm/s)	Residence Time (s)	Residence Time (days)	Residence Time (days)	Residence Time (days)
DaG 476											
Olivine											
		3°C/hr				0.4^{o}C/hr				10^{-7} mm/s	10^{-8} mm/s
	large	200	3.13E-07	1.45E+06	16.8	1250	5.00E-08	9.09E+06	105.2	52.6	526.1
	medium			4.48E+05	5.2			2.80E+06	32.4	16.2	162.1
	small			9.21E+04	1.1			5.76E+05	6.7	3.3	33.3
Pyroxene		200	1.32E-07	6.52E+05	7.5	1250	2.11E-08	4.07E+06	47.1	10.0	99.5
EET-A		5 ^{o}C/hr				0.4^{o}C/hr					
Olivine	large	120	5.44E-07	9.68E+05	11.2	1250	5.22E-08	1.01E+07	116.6	60.9	609.2
	small			6.58E+04	0.8			6.85E+05	7.9	4.1	41.4
Pyroxene		120	2.66E-07	3.50E+05	4.1	1250	2.56E-08	3.65E+06	42.2	10.8	108.0
Dho 019		0.1^{o}C/hr				0.05^{o}C/hr					
Olivine	large	5000	1.00E-08	1.68E+07	193.9	10000	5.00E-09	3.35E+07	387.7	19.4	193.9
	small			3.19E+06	36.9			6.38E+06	73.8	3.7	36.9
		0.8^{o}C/hr				0.5^{o}C/hr					
	large	625	8.00E-08	2.09E+06	24.2	1000	5.00E-08	3.35E+06	38.8		
	small			3.99E+05	4.6			6.38E+05	7.4		

The range of cooling rates for DaG 476 from 0.4 ^{o}C/hr (1200-700 ^{o}C) to 3 ^{o}C/hr (1300-700 ^{o}C) determined by Mikouchi *et al*. (2001) results in a range of growth times from 1250 to 200 hrs, respectively (Table 2). An average growth rate was calculated using these growth times and the average grain size for olivine (0.23 mm) and pyroxene (0.10 mm). Overall, the calculated average growth rates suggest that pyroxene may have crystallized slightly faster ($1.32 \times 10^{-7} – 2.11 \times 10^{-8}$ mm/s) than olivine ($3.13 \times 10^{-7} – 5.0 \times 10^{-8}$ mm/s). Though slightly faster, these growth rates are within an order of magnitude of the previously estimated growth rates ($1.68 \times 10^{-8} – 8.40 \times 10^{-8}$ mm/s) for similar silicate minerals in the Zagami shergottite (Lentz and McSween, 2000). The average slope of each linear segment of the CSD was used to calculate residence times for the three proposed olivine populations in DaG 476. Residence times for olivine decrease with decreasing grain size. A comparison of these data to the pyroxene residence times suggests that the pyroxene population began crystallizing before and then simultaneously with the intermediate-size olivines. The short residence times (1.1-6.7 days) and increased population density (Figure 4a) for the smallest olivine grains suggest this population may be the result of increased nucleation and rapid cooling upon eruption of the magma. The large range of residence times for the megacryst population (16.8-105.2 days) does not provide any conclusive evidence as to whether the population is phenocrystic or xenocrystic.

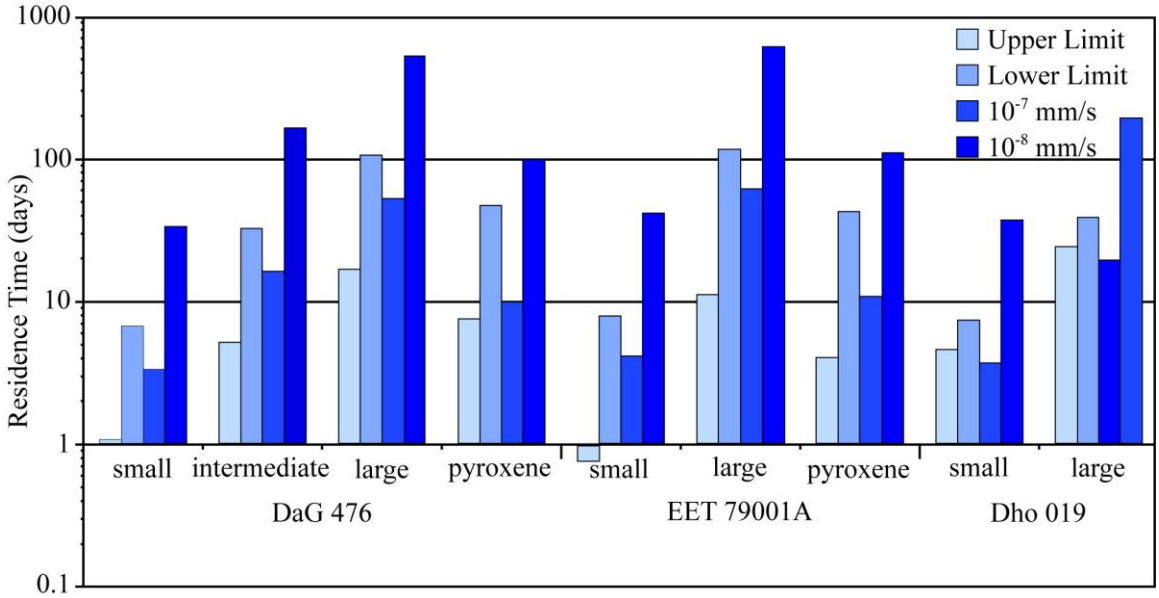

Figure 6. A comparison of residence times calculated for the individual crystal populations in DaG 476, EET 79001A, and Dho 019.

Observations for EET 79001A were similar to those made for DaG 476. The lower limit on cooling rate (0.4 ^{o}C/hr from 1200 to 700 ^{o}C) is the same as that determined for DaG 476 (Mikouchi *et al*., 2001), and yields comparable average growth rates, based on the similar average grain sizes of the olivine (0.24 mm) and pyroxene (0.12 mm) grains. The upper limit of 5°C/hr for the cooling rate, over a temperature interval of 1300-700 ^{o}C (Mikouchi *et al*., 2001), produces faster growth times and therefore faster average growth rates for olivine (5.44 x 10^{-7} mm/s) and pyroxene (2.66 x 10^{-7} mm/s) when compared to DaG 476. The overall shallower CSD slopes for EET 79001A produce shorter residence times for pyroxene regardless of growth rate; however, at the lower limit (0.4 ^{o}C/hr) the olivine populations exhibit longer residence times compared to DaG 476 olivine at the same cooling rate. This contrasts with the data of Lentz and McSween (2000), where the shallower slope for EET 79001A pyroxene grains resulted in

longer residence times compared to DaG 476 pyroxenes. Their residence times were calculated using slower growth rates derived for Zagami-like samples and the same upper and lower cooling rate limits (0.1-3 ^{o}C/hr) were applied to both samples, whereas this study utilized different cooling rates limits and therefore different growth rates for the two samples.

The olivine in Dho 019 has the smallest average grain size (0.18 mm) and the slowest cooling rates, ranging from 0.05-0.1 ^{o}C/hr over a temperature interval of 1200-700 ^{o}C (Mikouchi and Miyamoto, 2002). The calculated average growth rates are slower than those determined for DaG 476 and EET 79001A. Consequently, despite the steeper slope for the larger population, the residence time estimates are longer for Dho 019. Taylor *et al*. (2002) suggested faster cooling rates (0.5-0.8 ^{o}C/hr) for Dho 019 olivine, which result in faster average growth times and shorter residence times (Table 2).

These data show that the estimated growth rate has a significant effect on the calculated residence time. Marsh (1988) suggested that terrestrial growth rates for common silicate minerals are similar at ~10^{-9} mm/s, an estimate that is slower than growth rates calculated for olivine-phyric shergottites in this study (~10^{-7} mm/s) and for basaltic shergottites (~10^{-8} mm/s) calculated by Lentz and McSween (2000). Using a constant growth rate for all samples to calculate residence times results in shorter residences for steeper slopes and longer residence times for shallower slopes, as predicted by CSD theory (Marsh, 1988; Cashman and Marsh, 1988; Higgins, 2006). The faster growth rate estimate (~10^{-7} mm/s), similar to those calculated in this study, produces residence times that are consistent with cooling times required to preserve the observed Fe-Mg zonation in the samples (Taylor *et al*., 2002; Mikouchi *et al*., 2001; Mikouchi and

Miyamoto, 2002). However, caution must be exercised when making such generalizations, as P zonation patterns in olivine grains suggest that growth rates are not constant throughout the crystallization history.

4.3 Spatial Distribution Pattern Analysis

The spatial distribution pattern analysis provides a quantitative textural description of the arrangement of a grain population within a sample, which can provide insight into the nucleation distribution within the magma. The nearest neighbor method utilized (Jerram *et al*., 1996) allows for differentiation between clustered versus randomly distributed grains in a population based on a calculated R value and the sample porosity. (Porosity for igneous samples is defined as the percentage of remaining melt at the time of crystallization of the phase of interest and therefore will be referred to as melt porosity.) Jerram *et al.* (2003) supplemented the technique with a contribution that allows for the distinction between touching and non-touching crystal frameworks. The combined result is four distinct fields (ordered touching framework, ordered non-touching framework, clustered touching framework, and clustered non-touching framework) on a plot of R versus % melt porosity (Figure 4f).

Based on the melt porosity of the samples, the calculated R-values for olivine in two thin sections of DaG 476 fall within the clustered non-touching framework field (Figure 4f). The calculated R value for olivine in Dho 019 also falls within the clustered non-touching framework field, consistent with the results of Taylor *et al*. (2002), although the no distinction between touching versus non-touching framework was previously made. Textural observations of the samples in thin section, coupled with their

classification as clustered non-touching frameworks, indicate that the olivine populations within DaG 476 and Dho 019 likely grew from clusters of nuclei as a result of heterogeneous nucleation or later accumulated in clusters via the agglomeration of early formed crystals. The agglomeration of early-formed crystals is supported by the high-P cores observed in Dho 019 olivine megacrysts (Figure 5b).

An R value was determined for the pyroxene population in one thin section each of DaG 476 and EET 79001A. The melt porosity and the R-values of the samples place them within the clustered touching framework portion of the plot (Figure 4f), indicating that the pyroxene crystals grew and accumulated in clusters rather than as randomly distributed individual grains. This observation is consistent with previous cluster analyses on pyroxenes in some terrestrial (Jerram *et al*., 2003) and lunar basalts (Day and Taylor, 2007).

4.4 Implications for Shergottite Crystallization

Each sample selected for this study has a different Mars ejection age based on cosmogenic nuclides, suggesting that they originated from three different locations on the Martian surface. While many similarities exist between the samples, compositionally and texturally, CSD and P mapping results show that they may actually have very different cooling histories.

4.4.1 DaG 476

Three linear regressions can be fit to the CSD plot for olivine in DaG 476, possibly indicating three separate olivine populations. Significant kinks in the CSD plot

suggest mixing of magma, changes in crystallization dynamics, or addition of crystals (Marsh, 1988; Higgins, 2006). The addition of olivine crystals is most plausible based on elemental zonation patterns in this sample.

The olivine megacrysts are included in the largest size fraction (> 0.79 x 0.57 mm) that has a very shallow slope (avg. -2.20) with residence times ranging from 16.8 to 105.2 days. Four large olivine grains constitute the olivine megacryst in Figure 7. Elemental zonation and the inclusion of chromite grains suggest two distinct growth histories for the cores and rims of these olivine grains. P-rich regions in olivine suggest the incorporation of P in excess of equilibrium partitioning during rapid crystal growth such that zoning patterns primarily record crystal-growth-rate variations (Milam-Barris *et al.*, 2008). The cores have no P zonation, which indicate a constant growth rate, and they contain abundant chromite inclusions. The rims of the olivine grains exhibit oscillatory P zonation, suggesting intermittent periods of rapid olivine growth, and contain no chromite grains. The change in growth rate may occur as a result of magma mixing or eruption; however, Milam-Barris *et al.* (2008) suggested that oscillatory zoning is not necessarily associated with an external forcing. Although previous work reports systematic zonation of Fe and Mg (Mikouchi *et al*., 2001), this olivine cluster suggests that the original zonation has been altered. While the rims of olivine in contact with the melt exhibit continuous oscillatory P zonation, the Fe-Mg zonation is not continuous where a portion of the rim contains Mg-rich olivine. The rims of adjacent olivines are also Mg-rich, with no evidence of Fe-rich olivine growth or oscillatory P zonation.

Figure 7. DaG 476 olivine megacryst. a) BSE image. b) Mg K_β x-ray map illustrates Mg-rich cores (red). c) P K_α x-ray map with no zonation in core and high-P (green-red) oscillatory bands on rims. The small olivine in the lower left has oscillatory zoning too and is relatively high in P (red-white). d) Cr K_α x-ray map illustrates the chromite rich cores in the olivine (small white grains). e) Crystal size distribution of olivine in DaG 476 with three linear segments representing three olivine populations. (Image colors are not directly scaled; warm colors represent higher abundances than cool colors.)

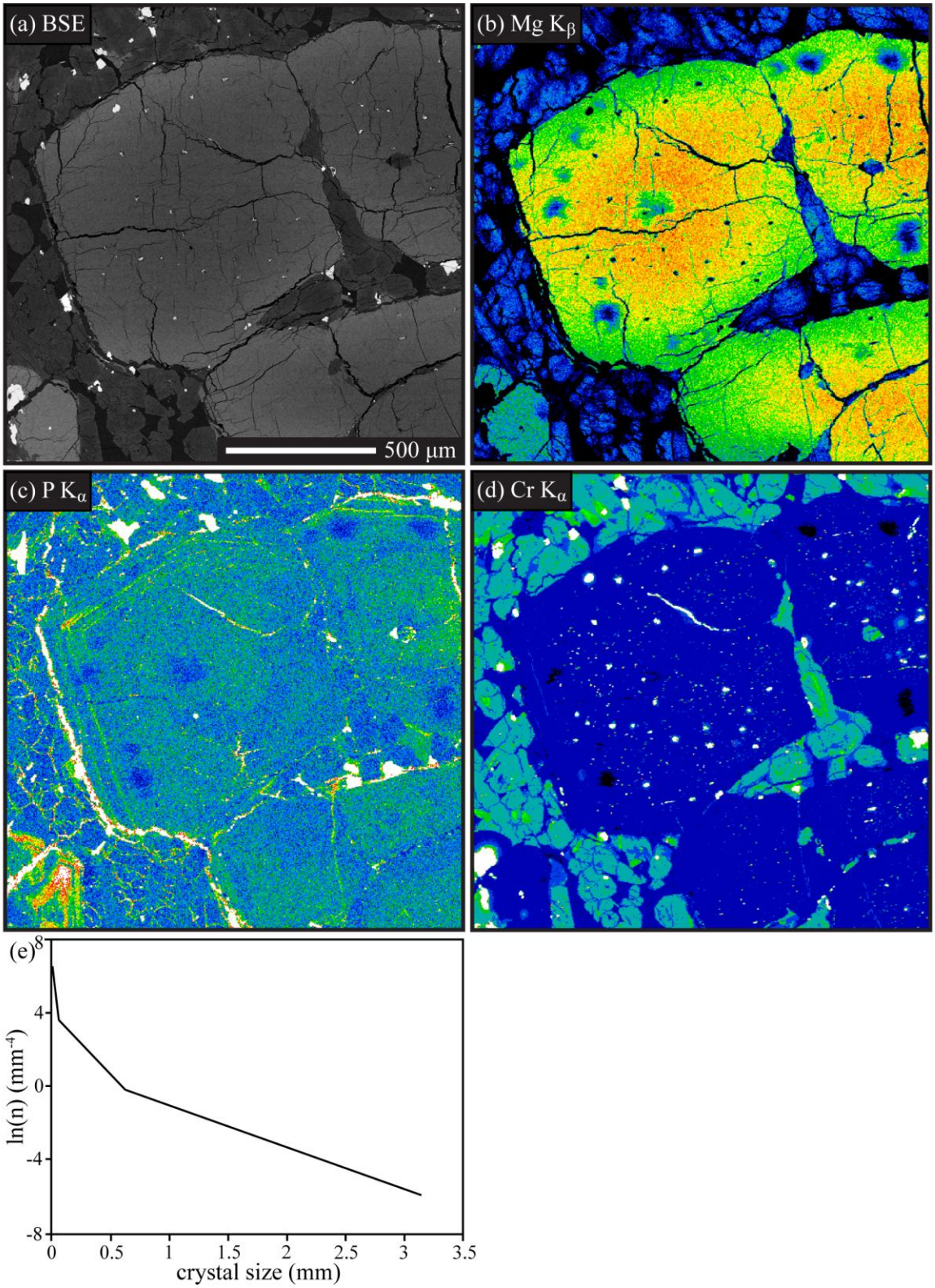

Figure 7. Continued.

A small individual, Fe-rich euhedral olivine grain, separate from the cluster, in the lower left corner of Figure 7, exhibits concentric oscillatory P zoning throughout the entire grain. This grain is approximately 0.4 x 0.25 mm, placing it in the intermediate-size olivine population with an estimated residence time of 5.2-32.4 days. This population likely represents the nucleation and growth of crystals during magma ascent. Based on the CSD data, pyroxenes crystallized before and concurrently with the intermediate-sized olivines, perhaps during magma ascent. The turnover for the pyroxenes, though, suggests that nucleation of pyroxene ceased and the smallest grains may have been resorbed via Oswald ripening.

The smallest olivine grain population (>0.09 mm), represented by the steepest slope (avg. -34.8) on the CSD plot, has the shortest residence time of 1.1-6.7 days (Table 2). The short residence time for this population and increase in nucleation rate, indicated by the increase in population density, suggest that this population might have grown in the lava flow after eruption. However, closer examination of this population in relation to the groundmass reveals another possible explanation for the abundance of small olivine grains. Many of the smallest grains are poikilitically enclosed by pyroxene grains; therefore, they may be the result of early-crystallized olivine that did not completely react to form pyroxene.

Overall, these data suggest that the olivine megacrysts grew from a more primitive melt. The chromite-bearing cores crystallized during an initial stage of olivine growth and accumulated in a crystal pile or along the walls of the magma chamber. The oscillatory P zoning, present on the rims of the olivine grains adjacent to the melt, suggests a second growth stage of chromite-absent olivine occurring after accumulation

of the grains. Fe-Mg zonation was nearly homogenized while the crystals resided in the cumulate pile. Ascent of a more evolved magma entrained the megacrysts, where they began to re-equilibrate with the melt as indicated by the high Fe rims. The small grains represent the earliest crystallized olivine remaining from reaction with the melt to form pyroxene that was present in the melt that entrained the megacrystic olivines. The Fe-rich, intermediate-sized olivines crystallized from this melt during ascent, accompanied by continued pyroxene nucleation and growth. Upon eruption, pyroxene nucleation ceased but growth continued.

4.4.2 EET 79001A

The CSD of EET 79001A is dominated by a single linear regression, indicating steady-state crystallization throughout most of the solidification history. Compared to the other samples, EET 79001A has the shallowest slope, with residence times ranging from 11.2-116.6 days. Liu *et al.* (2013) observed weak Mg zoning in the cores of olivines, suggesting that the olivines either experienced re-equilibration with the melt or grew slowly. The center of the megacryst in Figure 8 is slightly higher in P; however, well-defined P zonation is not evident. This observation supports a slow constant slow growth rate and consequently residence times on the order of 100 days. Longer residence times would allow for re-equilibration of the olivine grains. Goodrich (2003) suggests that the olivine megacrysts in EET 79001A experienced different growth rates throughout their history based on the location of melt inclusions in olivine mantles. The presence of melt inclusions indicates rapid growth to allow for the trapping of the melt. No high-P region is located in the olivine adjacent to observed melt inclusions in this sample. Subtle P

zonation is present in the smaller subhedral grain in Figure 8; this grain does indicate a change in growth rate during crystallization when compared the megacrysts.

Figure 8. EET 79001A olivine megacryst. a) BSE image. b) Mg K_β x-ray map illustrates Mg-rich core (red). c) P K_α x-ray map with high-P in core, but no well-defined zonation (green-yellow). The small olivine in the upper right is low in P, but has faint sector zoning (bluish white). d) Cr K_α x-ray map illustrates the chromite rich cores in the olivine (small red grains). e) Crystal size distribution of olivine in EET 79001A with two linear segments indicating steady state conditions for much of the cooling history. (Image colors are not directly scaled; warm colors represent higher abundances than cool colors.)

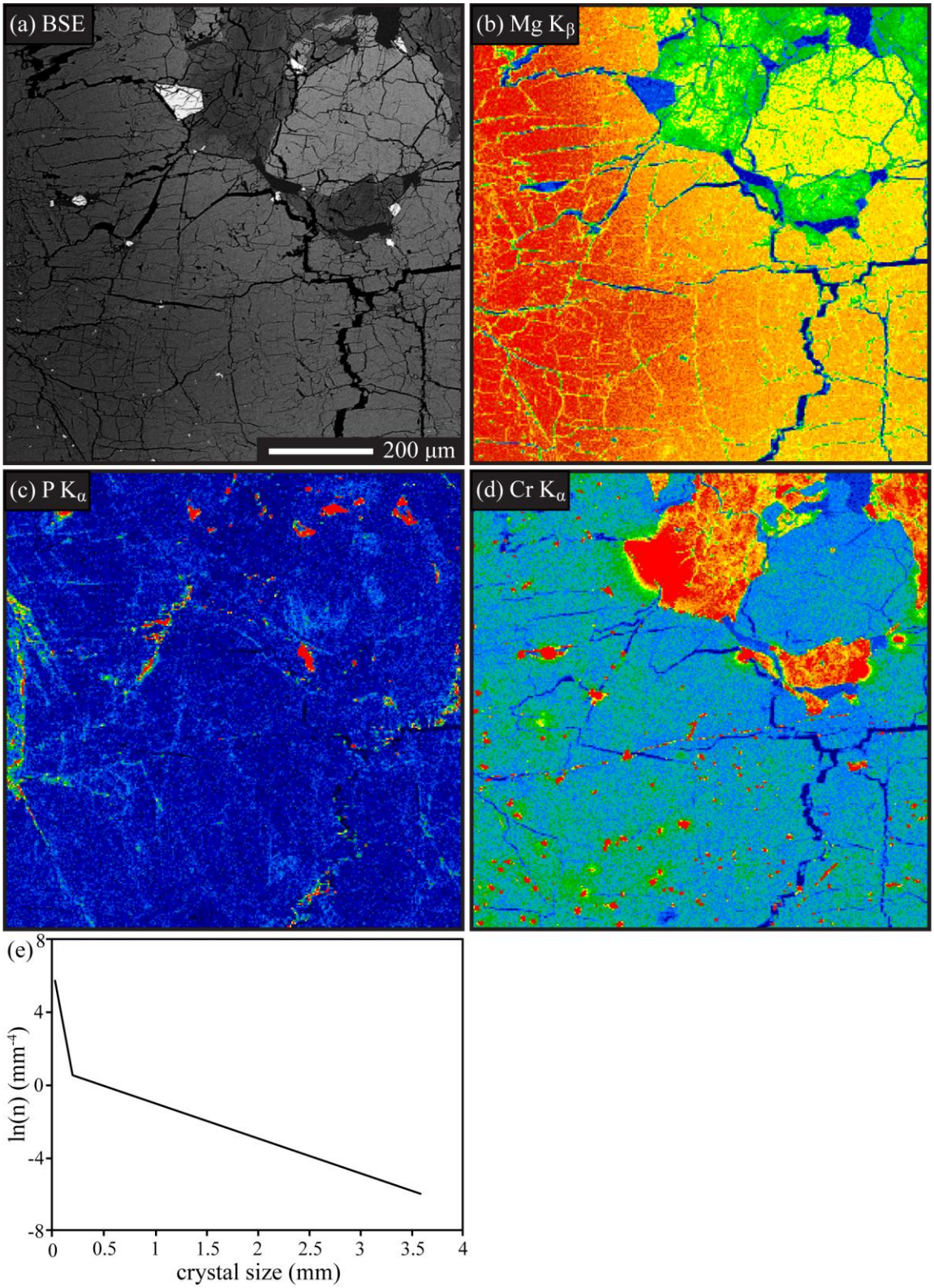

Figure 8. Continued.

In the ongoing debate on the origin of the megacrysts, Goodrich (2003) and Liu *et al*. (2013) agreed that the olivine population contains megacrysts of both xenocrystic and phenocrystic origin, but in differing proportions. Unfortunately, the CSD does not provide any further insight into this discussion. The CSD is linear over nearly the entire crystal population; however, there is a pronounced kink where a second linear regression can be fit at the smallest grain sizes (approximately > 0.4 mm). A "kinked" CSD suggests two crystal populations resulting from a two-stage cooling history, magma mixing, or addition of megacrysts. The addition of megacrysts is consistent with the observations of Goodrich (2003) and Liu *et al.* (2013). However, the kink occurs at a grain size too small to represent the megacryst population. Closer examination of the texture of the sample reveals that the smallest olivine grains are typically located near megacrysts that have been fragmented due to shock, or near grains that have irregular shapes indicating that they may have been resorbed by the melt (McSween and Jarosewich, 1983). Therefore, the increased population density at small crystal sizes may not provide a true representation of the crystallization processes, and the addition of a xenocrystic population is not evident in the CSD.

The single linear trend in the pyroxene CSD for EET 79001A suggests a continuous single-stage cooling history with residence times of 4.1-42.2 days. The single-stage cooling is consistent with zoning trends observed that suggest crystallization proceeded without interruption (Goodrich, 2003). These residence times are shorter than those for the megacryst olivines, supporting the onset of pyroxene after the growth or addition of olivine.

4.4.3 Dho 019

The overall shape of the corrected 3D CSD for the olivine population in Dho 019 is similar to the 2D CSD reported by Taylor *et al.* (2002). Like EET 79001A, the dominant linear segment of the CSD indicates steady-state conditions for much of the cooling history (Figure 4e). The slope of the olivine CSD is not as shallow as the slope for EET 79001A and is more similar to the slope at intermediate size for DaG 476 (Table 2). Residence times were calculated to be in the range of 24 to 388 days, depending on the cooling rate estimate.

A kink present at the small crystal sizes (approximately > 0.1 mm) suggests a change in crystallization dynamics to produce a second olivine population, perhaps associated with an increase in nucleation upon eruption. In EET 79001A, textural observations suggest the second population may be the result of megacryst fracturing or remnants of unreacted olivine in pyroxene. In Dho 019, however, the low Fo content of small homogeneous olivine grains (Mikouchi and Miyamoto, 2002) and residence times of 5 to 74 days calculated from the steep slope of the CSD support the nucleation and growth of olivine upon ascent and eruption.

Although the linear olivine CSD suggests steady-state conditions, a variety of P zonation patterns were observed (Figure 5, Figure 9), where two dominant patterns suggest different growth histories for the megacryst population. The olivine glomerocryst in Figure 8 (and Figure 5b) contains two high-P regions in the core with no apparent correlation to Cr or Fo content (Figures 5a, b, c). These high-P cores may represent a period of rapid olivine growth after a delay in nucleation due to undercooling (Milam-Barris *et al.*, 2008). The irregular shape of the high-P cores suggests resorption.

Subsequently, they acted as nucleation sites during a period of relatively slow crystallization (low-P olivine), during which time the grains grew together forming a glomerocryst. The olivine rim contains two high-P bands that are positively correlated with Cr. This correlation along the rim suggests a much shorter residence time for the rim compared to that of the core, which shows no correlation between P and Cr. High-P oscillatory zoning along the rim may represent a period of rapid growth, perhaps associated with eruption, similar to observations made for DaG 476 (Figure 7c). The presence of many previously unidentified glomerocrysts is consistent with the cluster analysis (Taylor *et al*., 2002).

Figure 9. Dho 019 olivine megacryst. a) BSE image. b) Mg K_β x-ray map illustrates reverse Mg-Fe zonation with high Mg on right most rim (red). c) P K_α x-ray map where high-P core (green) shows evidence of resorption and oscillatory P-rich bands are present on the rims. d) Cr K_α x-ray map illustrates the chromite rich core in the olivine on the right (small green-red grains). e) Crystal size distribution of olivine in Dho 019 with two linear segments representing two olivine populations. (Image colors are not directly scaled; warm colors represent higher abundances than cool colors.)

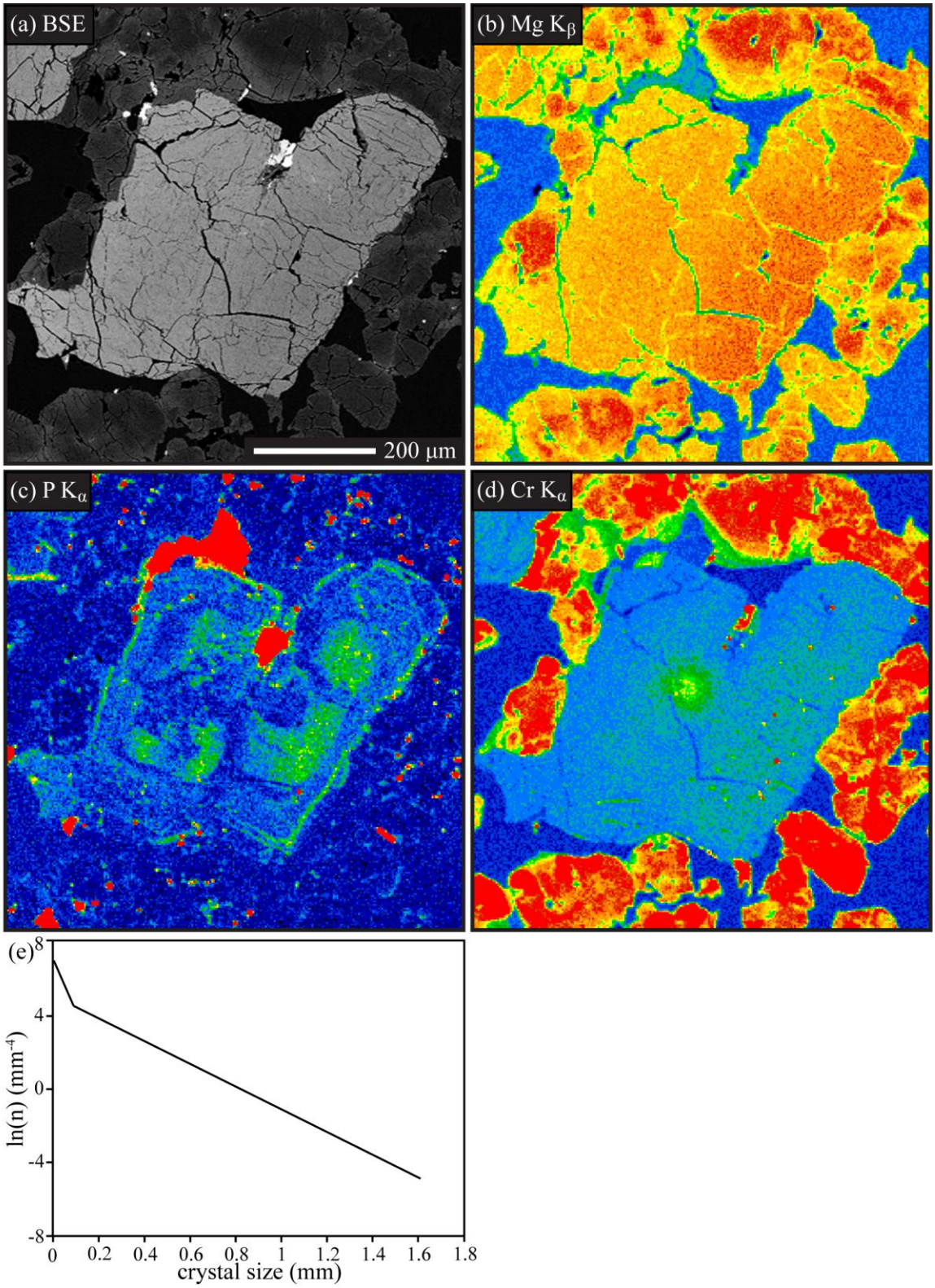

Figure 9. Continued.

Sector zoning around high-P melt inclusions is the second pattern that is common in the Dho 019 olivines. P-rich melt inclusions are often located in regions of high-P olivine, with the olivine directly adjacent to the melt inclusions being depleted in P and Cr (Figure 5i). The occurrence of melt inclusions (Figure 5g) within the olivine grains supports rapid growth, where the high-P olivine is not in equilibrium with the melt. Some dissolution of the P-rich olivine then occurred when in contact with a melt inclusion. This was then followed by slow reprecipitation of olivine, resulting in low-P olivine halos around the melt inclusions. The high-P skeletal pattern in the olivine megacryst in Figure 5 is also indicative of rapid olivine growth, reflecting "solute trapping", where the P-enriched olivine was not in equilibrium with the melt (Milam-Barris *et al*., 2008).

Mg-Fe zonation varies greatly throughout the sample, in which some crystals exhibit reverse zonation (Figure 5a, Figure 9b), some are homogeneous (Figure 5j), and some have normal zonation (Figure 5g) with rim compositions similar to the small olivine population. Glomerocrysts tend to have high-P cores that show evidence of resorption, and large single grains exhibit sector zoning. Interestingly, the glomerocrysts tend to be reversely zoned with respect to Mg-Fe, while the sector zoned olivines exhibit normal zoning. Reverse Mg-Fe zonation present in the glomerocrysts suggest longer residence times for these grains. Overall, the P zoning patterns within the olivine of Dho 019 suggest alternating rapid and slow growth, punctuated by periods of grain dissolution (Figure 9c). Therefore, caution must be exercised when considering residence times calculated using constant growth rates.

Crystallization was previously modeled using the MELTS program (Taylor *et al.*, 2002), and those results suggested that crystallization was likely close to fractional, where crystals were separated from the magma after they grew. The interpretation of the modeling results suggests that some fractionation of the magma resulted through isolation of growing crystals and restriction of diffusive exchange during cooling and crystallization (Taylor *et al.*, 2002). The agglomeration of early-crystallized olivine (Fig. 5b, 9c) may have aided in fractionation of the melt. The high-P olivine nuclei may have experienced a period of slow-growth (low-P olivine) while residing in an area of accumulated olivine, perhaps in a crystal pile or along the walls of a magma chamber. This model is consistent with the SDP analysis that suggests the olivine grains grew from clusters of nuclei or accumulated in clusters, rather than as individual, randomly distributed grains.

4.5 Origin of Megacrysts

Compositional and textural studies have debated the origin of the olivine megacrysts in olivine-phyric shergottites (Balta *et al.*, 2013; Goodrich, 2003; Liu *et al.*, 2013; McSween and Jarosewich, 1983; Walton *et al.*, 2005; Zipfel *et al.*, 2000). The use of stereographically corrected CSDs and elemental zonation maps, in conjunction with previous work, provides further insight into this debate.

The kink present in the olivine CSD in DaG 476 indicates changes in crystallization or addition of a second population. Modeling of DaG 476 as a mixture of known lherzolitic and basaltic composition led to the conclusion by Zipfel *et al*. (2000) that the olivines are most likely phenocrystic in origin as the *mg#* and abundance of many

trace elements are nearly as high as those in lherzolitic shergottites. Mikouchi *et al.* (2001) and Wadhwa *et al.* (2001) argued that the olivine crystallizing from the bulk rock should be more Mg-rich than is observed in the final rock. One possible explanation for the kink observed in the CSD, that is consistent with elemental data, is that the megacrysts are antecrysts. "Antecryst" is a term used to describe megacrysts that crystallized from a liquid similar to the groundmass, but resided in a cumulate pile for a significant period of time before entrainment upon eruption (Balta *et al*., 2013). The chromite-bearing olivine cores could have crystallized from a more Mg-rich magma and settled into a cumulate pile where subsequent olivine growth occurred. Long residence time in the cumulate pile would have allowed for the diffusive exchange of Mg-Fe to produce the homogenization observed in the megacrysts. These megacrysts may then have been entrained in a more evolved melt upon eruption, during which time the intermediate olivine crystals grew and the megacryst rims re-equlibrated with the more Fe-rich magma. Therefore, the kink is produced through the entrainment of large olivine antecrysts that experienced continued growth during residence within a cumulate pile.

Using the old methodology, previous analyses of the olivine population in EET 79001A and Dho 019 produced CSDs with a horizontal leveling at the larger size fraction that suggested the addition of megacrysts (Goodrich, 2003; Taylor *et al.*, 2002). The stereographically corrected CSDs, however, have a single linear trend over much of the crystallization history of EETA 79001A and Dho 019, indicating steady-state crystallization in a closed system with no loss or accumulation of crystals.

McSween and Jarosewich (1983) observed strong Mg-Fe zonation in EET 79001A olivine megacrysts, and suggested that the grains might be disaggregated

xenoliths of harzburgite with relict zonation, as they are not in equilibrium with the host. Later petrogenic modeling based on the composition of melt inclusions in the olivine grains suggested that only a small fraction of the megacrysts were xenocrysts (Goodrich, 2003). Based on REEs and recently determined partition coefficients for martian magmas, Liu *et al.* (2013) found that even the most Mg-rich olivine cores actually are in equilibrium with the melt, though it is unclear if they are actually phenocrysts or if they have re-equilibrated with the melt. Only 0-1.9% of the olivine megacrysts are xenocrysts based on rounded and irregular boundaries observed in X-ray maps (Liu *et al*., 2013). The CSD results and textural observations of this study support the conclusion that only a small fraction of the megacrysts in EET 79001A are xenocrystic.

No kink is present in the olivine CSD for Dho 019 to indicate mixing of two olivine populations or different crystallization histories; however, element zonation observed within the sample suggests otherwise. Glomerocrysts tend to have high P-cores and exhibit reverse Mg-Fe zonation, whereas large single crystals have sector P zonation and are normally zoned. The reverse zonation suggests the glomerocrystic olivines have experienced longer residence times than the single crystals in which the original Mg-Fe zonation may be preserved. The small homogeneous olivine population shows a large range in Mg-Fe composition and, similar to some of the megacrysts, they are too Fe-rich to be in equilibrium with the groundmass melt (Mikouchi and Miyamoto, 2002). These observations suggest that the Fe-rich glomerocrysts and Fe-rich small-grainsize population may have mixed with a more Mg-rich melt just prior to eruption in order to retain the original zonation preserved in the normally zoned single crystals. Interestingly, this is not recorded in the slope of the CSD. The lack of a significant kink in the CSD

data may be due to the similarities in grain size of the two mixed populations; therefore it is important to consider all types of data when interpreting CSDs.

CHAPTER V

CONCLUSIONS

This textural study re-evaluates the CSD of early crystallizing minerals (olivine and pyroxene) in DaG 476, EET 79001A, and Dho 019, using new stereographically corrected methods. SDP analysis was used to evaluate clustering of olivine and pyroxene. These textural methods were used in conjunction with elemental X-ray maps of olivine grains to ascertain information about the crystallization histories of these meteorites, thought to have been launched from three different localities on the martian surface. P zonation in olivine has revealed growth processes that may have otherwise been erased during long residence times within the magma chambers. These studies indicate the following:

- A comparison of the stereographically corrected CSDs to those previously reported that used the Wager method to correct for length versus area grain measurements show that the new methodology produces similar slopes but different intercepts, as seen in the olivine population of EET 79001A. However, comparison of the new data with analyses made using the old methodology, but without any correction from length to area, shows large variation in slope, with similar intercepts.
- The calculation of residence times requires the assumption of a constant growth rate, yet P zonation maps reveal that growth rates within these samples were not constant. Therefore a range of growth rates must be used and caution must be exercised when discussing calculated residence times.

- SPD analysis shows the pyroxene populations in both DaG 476 and EET 79001A are clustered, touching frameworks, indicating that the crystals grew or accumulated in clusters rather than as randomly distributed grains. The olivine populations in DaG 476 and Dho 019 were determined to be clustered, non-touching frameworks.
- The linear CSDs for the pyroxene populations in DaG 476 and EET 79001A indicate nucleation and growth under steady-state conditions throughout much of the crystallization histories.
- DaG 476 may contain up to three olivine size populations. The megacryst population, interpreted as antecrysts, possibly grew from a melt similar in composition (but perhaps more Mg-rich) to the groundmass, and resided in a cumulate pile that experienced continued growth before entrainment and eruption. An intermediate-sized population likely grew during magma ascent and eruption. A small population is likely unreacted olivine poikilitically enclosed in pyroxene.
- EETA 79001, the most recently ejected Martian meteorite, contains a single olivine population as indicated by the linear CSD. The low slope indicates a long residence time for the megacrysts that may be phenocrysts or antecrysts. Only a small fraction of the population are xenoliths.
- Dho 019, representing the earliest ejected Martian rock, has a complex history. Despite the linear CSD for olivine, Mg-Fe and P zonation patterns suggest mixing of two crystal populations.

CSD and SDP analysis are valuable tools that can be used to quantify the texture of igneous samples. For more accurate interpretation, it is essential the textural data be considered with compositional data.

LIST OF REFERENCES

Armienti P., Pareschi M. T., Innocenti F. and Pompilio M. (1994) Effects of magma storage and ascent on the kinetics of crystal growth. *Contributions to Mineralogy and Petrology* **115**: 402-414.

Balta J. B., Sanborn M., McSween H. Y. and Wadhwa M. (2013) Magmatic history and parental melt composition of olivine-phyric shergottite LAR 06319: Importance of magmatic degassing and olivine antecrysts in Martian magmatism. *Meteoritics & Planetary Science* **48:** 1359-1382.

Beckett J. R., McCanta M. C. and Stopler E. M. (2008) Phosphorus zoning in SNC olivines. *Lunar and Planetary Science Conf.* **XXXIX** *Abs.* 1726.

Cashman K. V. and Marsh B. D. (1988) Crystal size distribution (CSD) in rocks and the kinetics and dynamics of crystallization II. Makaopuhi Lava Lake. *Contributions to Mineralogy and Petrology* **99**: 292-305.

Clark P. J. and Evans F. C. (1954) Distance to nearest neighbor as a measure of spatial relationships in populations. *Ecology* **35**: 445-453.

Day J. M. D. and Taylor L. A. (2007) On the structure of mare basalt lava flows from textural analysis of the LaPaz Icefield and Northwest Africa 032 lunar meteorites. *Meteoritics & Planetary Science* **42**: 3-17.

Folco L., Franchi I. A., D'Orazio M., Rocchi S. and Schultz L. (2000) A new martian meteorite from the Sahara: The shergottite Dar al Gani 489. *Meteoritics & Planetary Science* **35**: 827-839.

Greshake A., Fritz J. and Stöffler D. (2004) Petrology and shock metamorphism of the olivine-phyric shergottite Yamato 980459: Evidence for a two stage cooling and a single-stage ejection history. *Geochimica et Cosmochimica Acta* **68**: 2359-2377.

Goodrich C. A. (2002) Olivine-phyric Martian basalts: A new type of shergottite. *Meteoritics & Planetary Science* **37**: B31-B34.

Goodrich C. A. (2003) Petrogenesis of olivine-phyric shergottites Sayh al Uhaymir 005 and Elephant Moraine A79001 lithology A. *Geochimica et Cosmochimica Acta* **67**: 3735-3771.

Higgins M. D. (1996) Magma dynamics beneath Kameni volcano, Thera, Greece, as revealed by crystal size and shape measurements. *Journal of Volcanology and Geothermal Research* **70**: 37-48.

Higgins M. D. (2000) Measurement of crystal size distributions. *American Mineralogist* **85**: 1105-1116.

Higgins M. D. (2006) *Quantitative textural measurements in igneous and metamorphic petrology*. Cambridge University Press, 270 pp.

Kirkpatrick R. J. (1977) Nucleation and growth of plagioclase, Mahaopuhi and Alae lava lakes, Kilauea volcano, Hawaii. *Geological Society of America Bulletin* **88**: 78-84.

Jerram D. A., Cheadle M. J., Hunter R. H. and Elliott M. T. (1996) The spatial distribution of grains and crystals in rocks. *Contributions to Mineralogy and Petrology* **125**: 60-74.

Jerram D. A., Cheadle M. J. and Philpotts A. R. (2003) Quantifying the building blocks of igneous rocks: Are clustered crystal frameworks the foundation? *Journal of Petrology* **44**: 2033-2051.

Lentz R. C. F. and McSween H. Y. (2000) Crystallization of the basaltic shergottites: Insights from crystal size distribution (CSD) analysis of pyroxenes. *Meteoritics & Planetary Science* **35**: 919-927.

Lentz R. C. F. and McSween H. Y. (2005) A textural examination of the Yamato 980459 and Los Angeles shergottites using crystal size distribution analysis. *Antarctic Meteorite Research* **18**: 66-82.

Liu Y., Balta J. B., Goodrich C. A., McSween H. Y., and Taylor L. A. (2013) New constraints on the formation of shergottite Elephant Moraine 79001 lithology A. *Geochimica et Cosmochimica Acta* **108**: 1-20.

Marsh B. D. (1988) Crystal size distribution (CSD) in rocks and the kinetics and dynamics of crystallization I. Theory. *Contributions to Mineralogy and Petrology* **99**: 277-291.

Marsh B. D. (1998) On the interpretation of crystal size distributions in magmatic systems. *Journal of Petrology* **39**: 553-599.

McCanta M. C., Beckett J. R. and Stopler E. M. (2008) Zonation of phosphorus in olivine: Dynamic crystallization experiments and a study of chondrule olivine in unequilibrated ordinary chondrites. *Lunar and Planetary Science Conf.* **XXXIX** *Abs.* 1807.

McCanta M. C., Beckett J. R. and Stopler E. M. (2009) Phosphorus zonation in H chondrite olivines: The effects of increasing petrologic grade. *Lunar and Planetary Science Conf.* **XL** *Abs.* 2048.

McCoy T. J. and Lofgren G. (1999) Crystallization of the Zagami shergottite: An experimental study. *Earth and Planetary Science Letters* **173:** 397-411.

McSween H. Y. (2008) Martian meteorites as crustal samples. In *The Martian Surface: Composition, Mineralogy, and Physical Properties* (ed. J. F. Bell III), pp. 381-396. Cambridge University Press, New York, New York, USA.

McSween H. Y. and Jarosewich E. (1983) Petrogenesis of the Elephant Moraine A79001 meteorite – multiple magma pulses on the sgergottite parent body. *Geochimica et Cosmochimica Acta* **47**: 1501-1513.

McSween H. Y., Stolper E. M., Taylor L. A., Muntean R. A., O'Kelley G. D., Eldridge J. S., Biswas S., Ngo H. T. and Lipschutz M. E. (1979) Petrogenetic relationship between Allan Hills 77005 and other achondrites. *Earth and Planetary Science Letters* **45:** 275-284.

Mikouchi T. and Miyamoto M. (2002) Mineralogy and olivine cooling rate of the Dhofar 019 shergottite. *Antarctic Meteorite Research* **15**: 122-142.

Mikouchi T., Miyamoto M. and McKay G. A. (2001) Mineralogy and petrology of the Dar al Gani 476 martian meteorite: Implications for its cooling history and relationship to other shergottites. *Meteoritics & Planetary Science* **36**: 531-548.

Milman-Barris M. S., Beckett J. R., Baker M. B., Hofmann A. E., Morgan Z., Crowley M. R., Vielzeuf D. and Stolper E. (2008) Zoning of phosphorus in igneous olivine. *Contributions to Mineralogy and Petrology* **155**: 739-765.

Mock A. and Jerram D. A. (2005) Crystal size distribution (CSD) in three dimensions: Insights from the 3D reconstruction of a highly porphyritic rhyolite. *Journal of Petrology* **46**: 1525-1541.

Morgan D. J. and Jerram D. A. (2006) On estimating crystal shape for crystal size distribution analysis. *Journal of Volcanologist and Geothermal Research* **154**: 1-7.

Peterson T. D. (1996) A refined technique for measuring crystal size distributions in thin section. *Contributions to mineralogy and petrology* **124**: 395-405.

Sahagian D. L. and Proussevitch A. A. (1998) 3D particle size distribution from 2D observations; stereology for natural applications. *Journal of Volcanology and Geothermal Research* **84**: 173-196.

Taylor L. A., Nazarov M. A., Shearer C. K., McSween H. Y., Cahill J., Neal C. R., Ivanova M. A., Barsukova L. D., Lentz R. C., Clayton R. N. and Mayeda T. K. (2002) Martian meteorite Dhofar 019: A new shergottite. *Meteoritics & Planetary Science* **37**: 1107-1128.

Wager L. R. (1961) A note on the origin of ophitic texture in the chilled olivine gabbro of the Skaergaurd intrusion. *Geological Magazine* **98**: 353-366.

Walton E. L., Spray J. G., and Bartoschewitz R. (2005) A new Martian meteorite from Oman: Mineralogy, petrology, and shock metamorphism of olivine-phyric shergottite Sayh al Uhaymir 150. *Meteoritics & Planetary Science* **40**: 1195-1214.

Zipfel J., Scherer P., Spettel B., Dreibus G. and Schultz L. (2000) Petrology and chemistry of the new shergottite DaR al Gani 476. *Meteoritics & Planetary Science* **35**: 95-106-1214.

APPENDIX

Appendix A

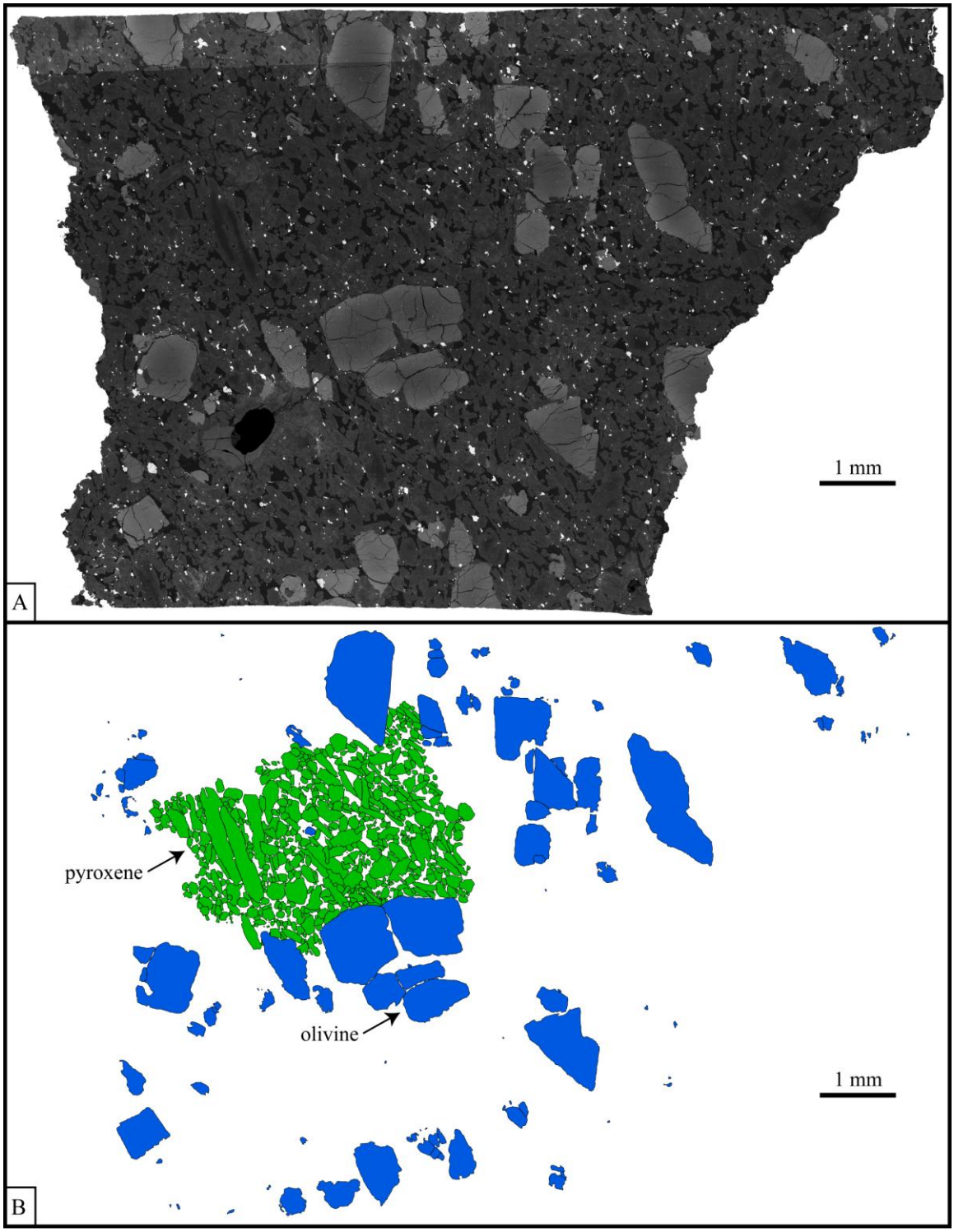

Figure 10. a) SEM image of DaG 476 thin section used to trace olivine and pyroxene grains. b) Olivine and pyroxene grain traces.

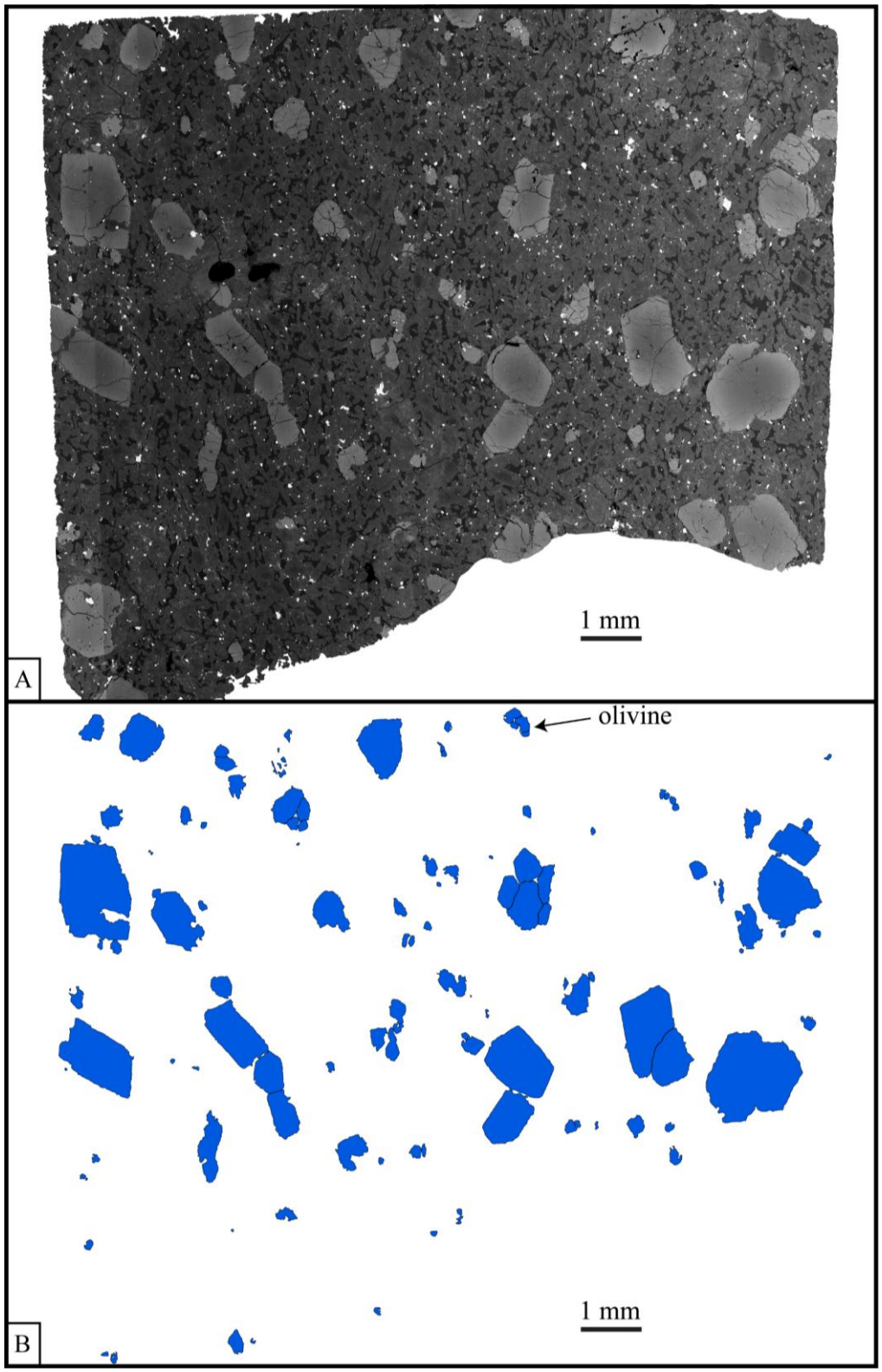

Figure 11. a) SEM image of second DaG 476 thin section used to trace olivine grains. b) Olivine grain traces.

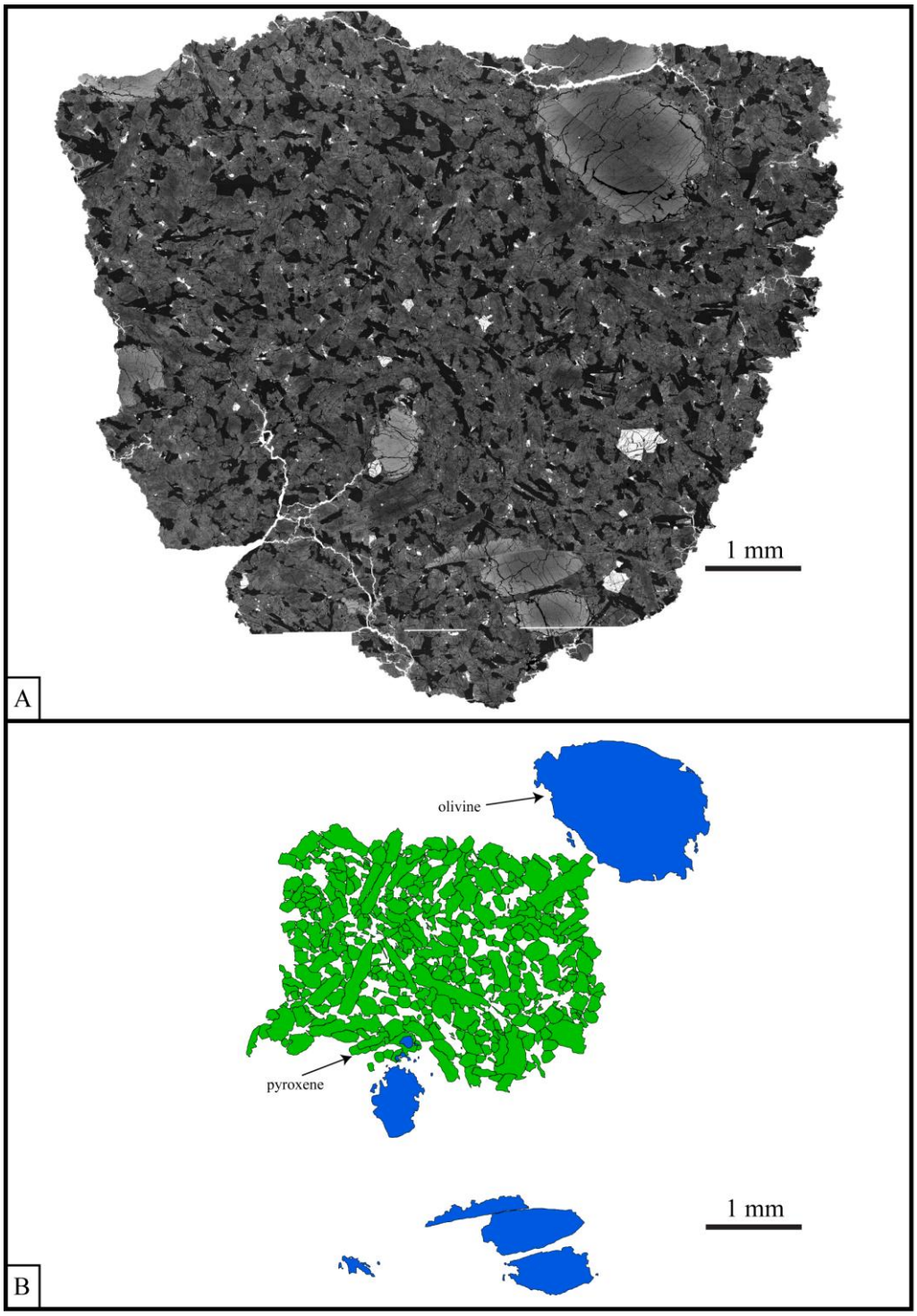

Figure 12. a) SEM image of EET 79001A thin section used to trace olivine and pyroxene grains. b) Olivine and pyroxene grain traces.

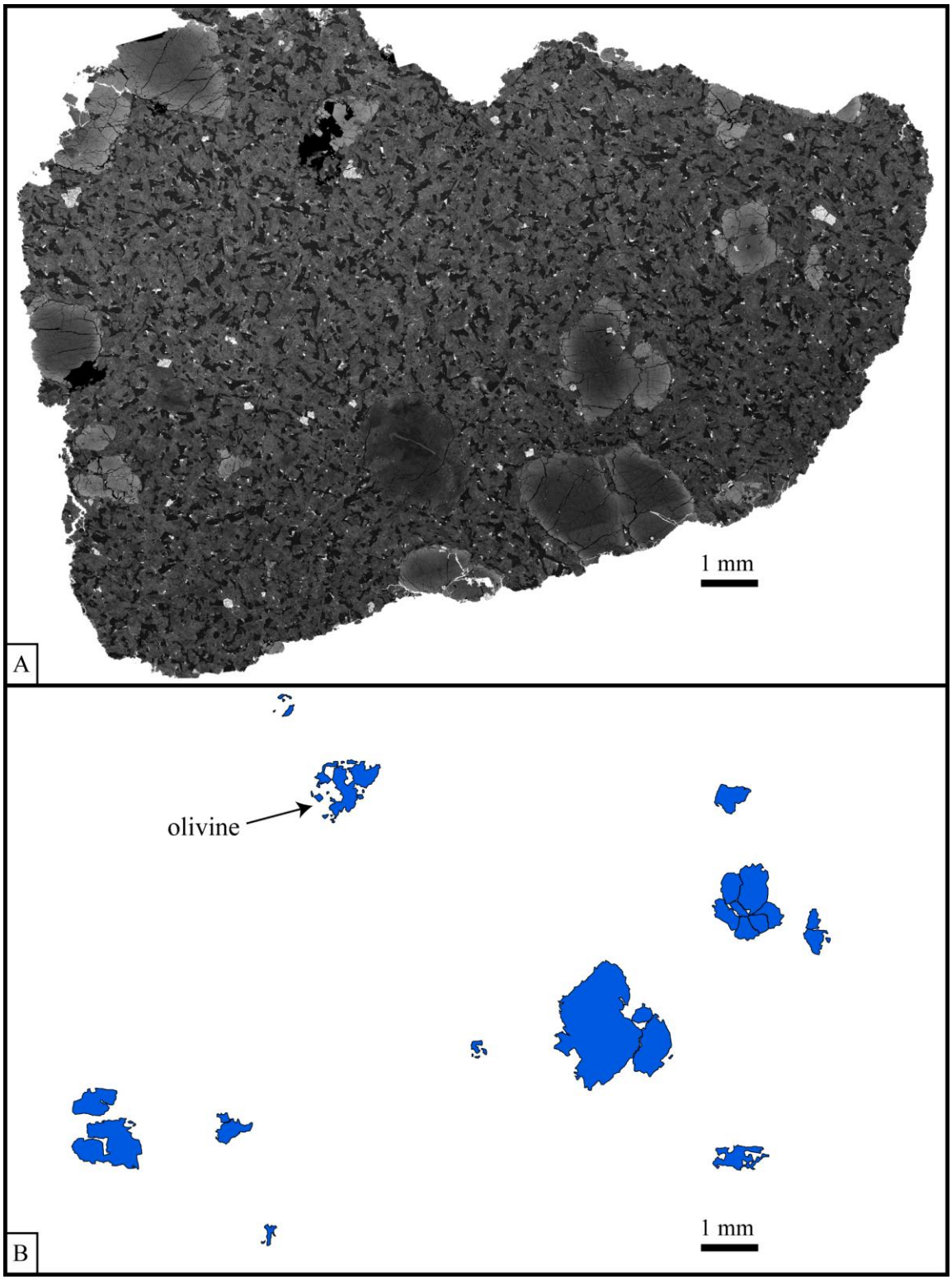

Figure 13. a) SEM image of EET 79001A thin section used to trace olivine grains. b) Olivine grain traces.

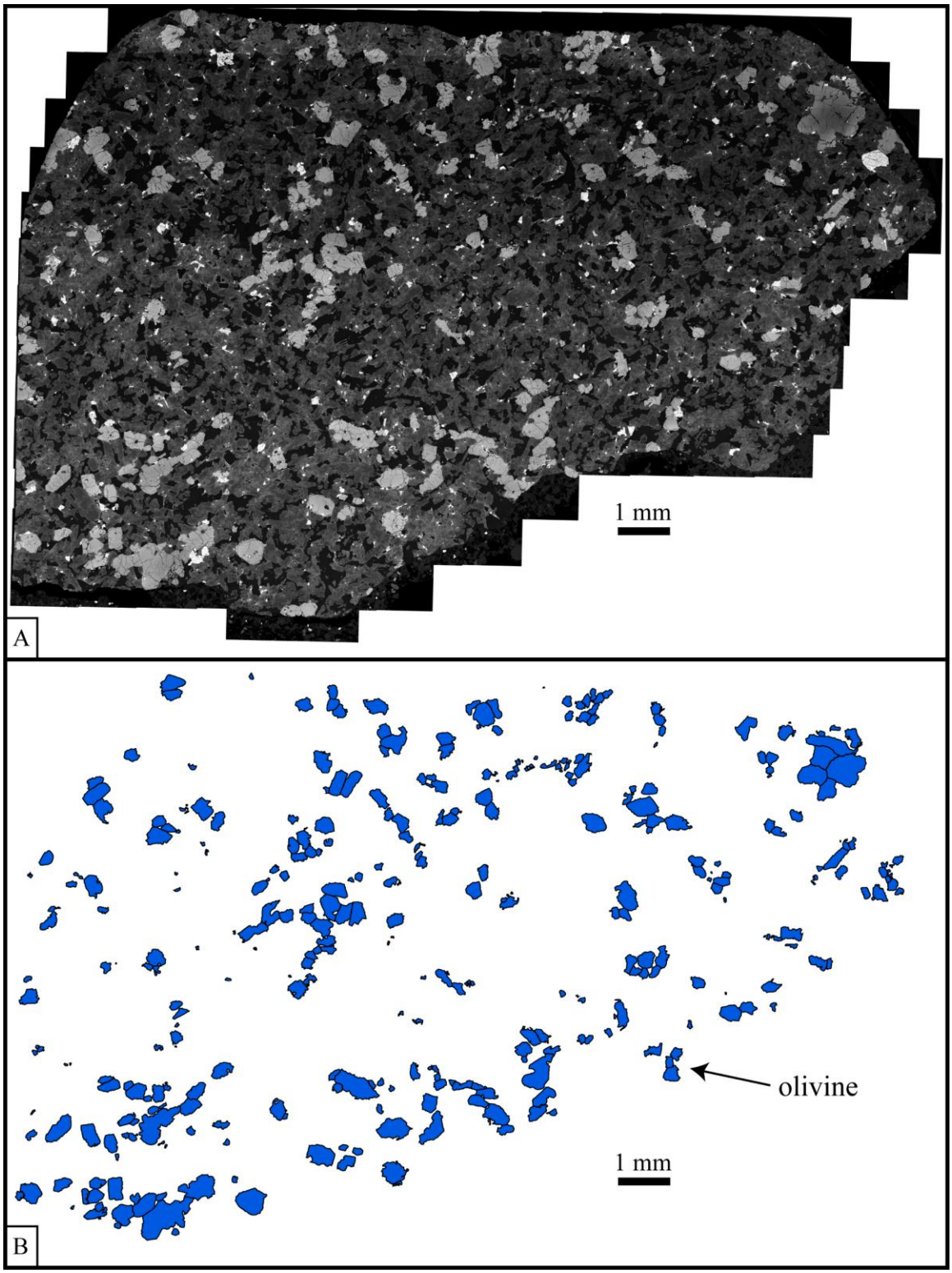

Figure 14. a) SEM image of Dho 019 thin section used to trace olivine grains. b) Olivine grain traces.

Appendix B

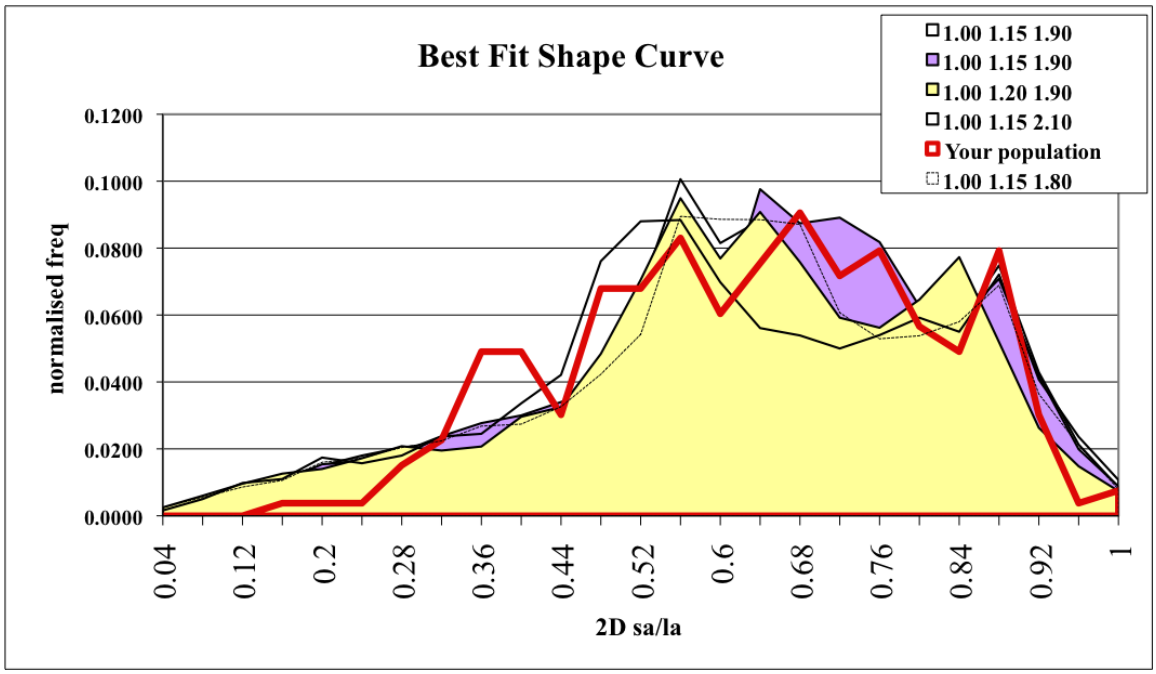

Figure 15. The five best-fit shape curves output from *CSD Slice* for DaG 476 olivine grains compared to the shape curve for the actual grain population (sa/la = short axis/long axis).

Table 3. Crystal habits for the five best-fit shape curves for DaG 476 olivine grains.

Shape	x	y	z	Score (R^2)
best	1.00	1.15	1.80	0.8078
2nd best	1.00	1.15	1.90	0.7882
3rd	1.00	1.15	1.60	0.7850
4th	1.00	1.20	1.90	0.7799
5th	1.00	1.15	2.10	0.7769

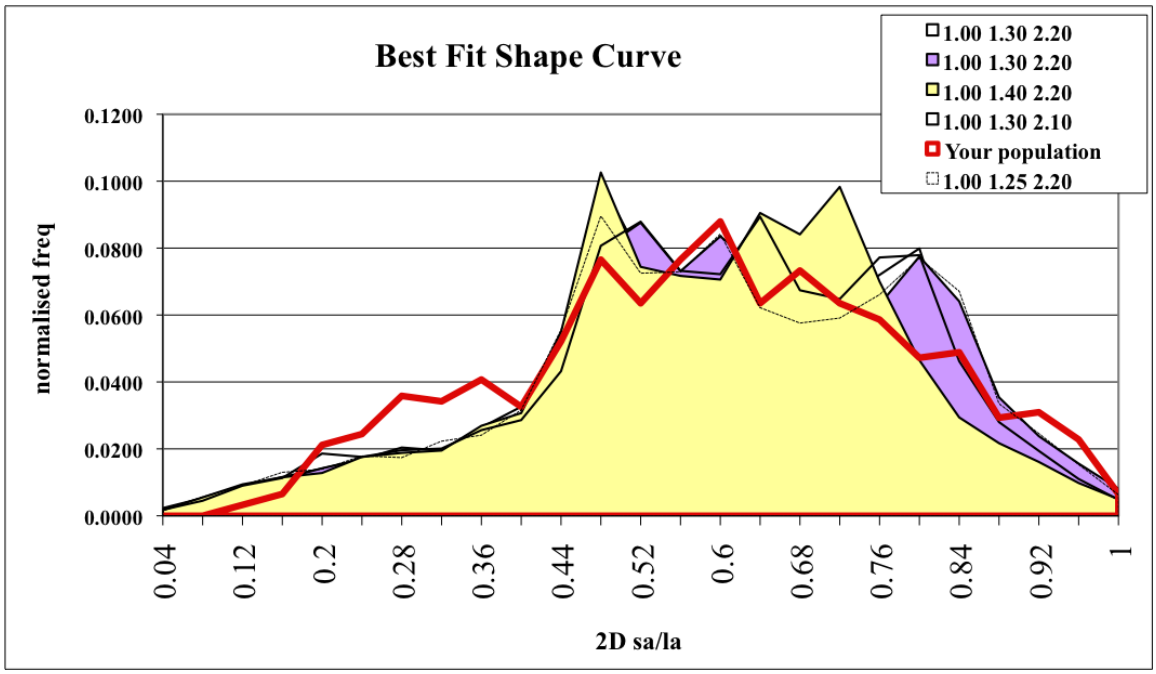

Figure 16. The five best-fit shape curves output from *CSD Slice* for DaG 476 pyroxene grains compared to the shape curve for the actual grain population (sa/la = short axis/long axis).

Table 4. Crystal habits for the five best-fit shape curves for DaG 476 pyroxene grains.

Shape	x	y	z	Score (R^2)
best	1.00	1.25	2.20	0.8503
2nd best	1.00	1.30	2.20	0.8467
3rd	1.00	1.25	2.10	0.8403
4th	1.00	1.40	2.20	0.8184
5th	1.00	1.30	2.10	0.8172

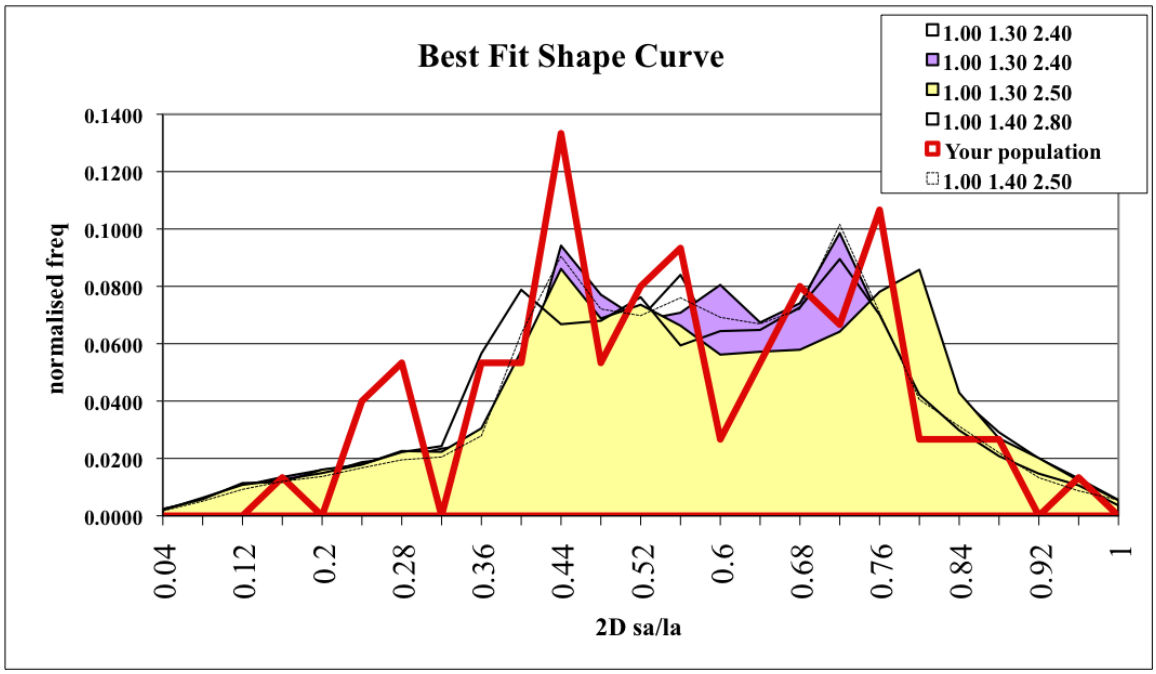

Figure 17. The five best-fit shape curves output from *CSD Slice* for EET 79001A olivine grains compared to the shape curve for the actual grain population (sa/la = short axis/long axis).

Table 5. Crystal habits for the five best-fit shape curves for EET 79001A olivine grains.

Shape	x	y	z	Score (R^2)
best	1.00	1.40	2.50	0.6843
2nd best	1.00	1.30	2.40	0.6482
3rd	1.00	1.40	2.40	0.6410
4th	1.00	1.30	2.50	0.6364
5th	1.00	1.40	2.80	0.6232

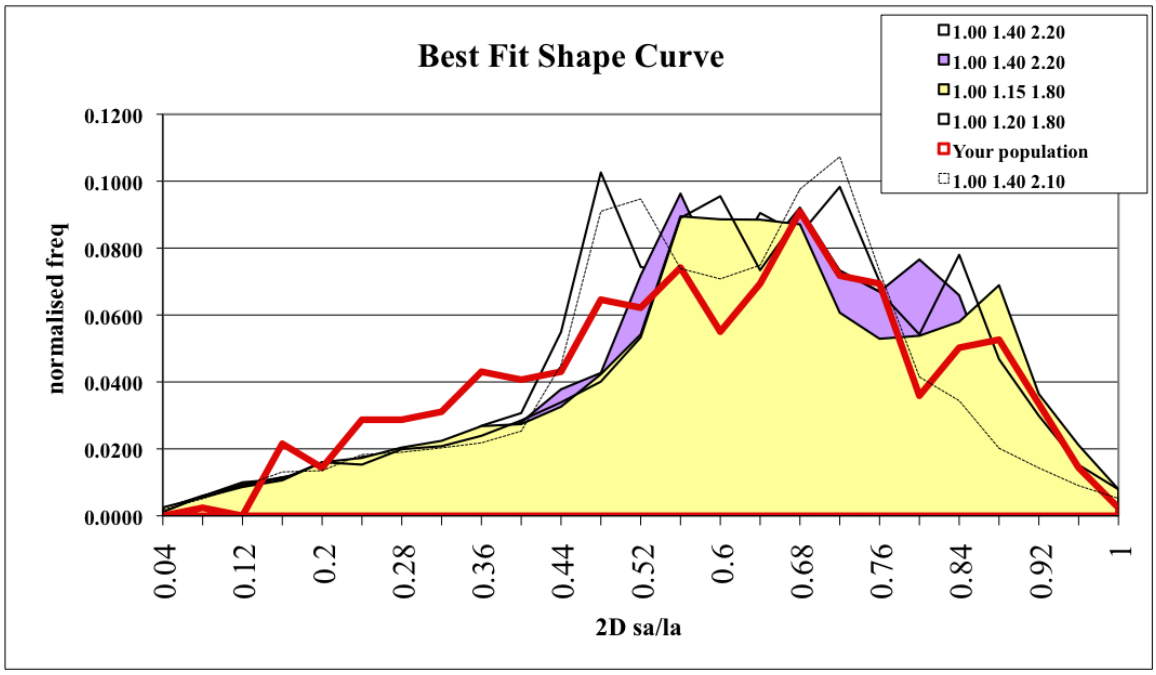

Figure 18. The five best-fit shape curves output from *CSD Slice* for EET 79001A pyroxene grains compared to the shape curve for the actual grain population (sa/la = short axis/long axis).

Table 6. Crystal habits for five best-fit shape curves for EET 79001A pyroxene grains.

Shape	x	y	z	Score (R^2)
best	1.00	1.40	2.10	0.7941
2nd best	1.00	1.40	2.20	0.7812
3rd	1.00	1.25	1.90	0.7806
4th	1.00	1.15	1.80	0.7726
5th	1.00	1.20	1.80	0.7690

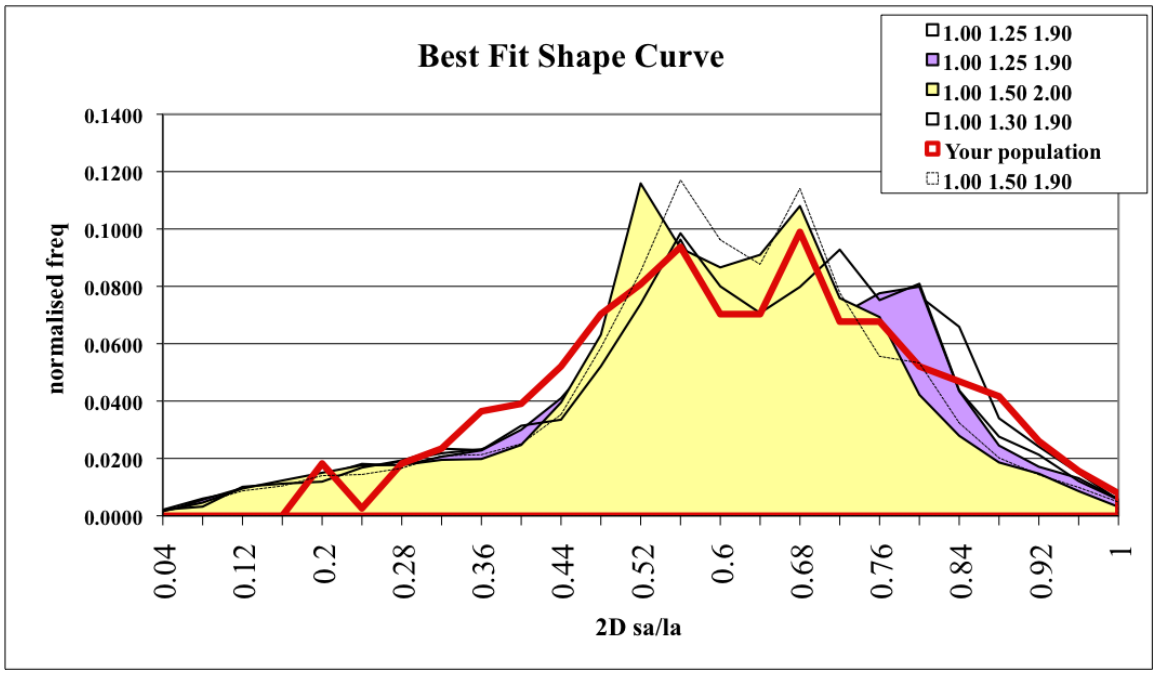

Figure 19. The five best-fit shape curves output from *CSD Slice* for Dho 019 olivine grains compared to the shape curve for the actual grain population (sa/la = short axis/long axis).

Table 7. Crystal habits for the five best-fit shape curves for Dho 019 olivine grains.

Shape	x	y	z	score (R^2)
best	1.00	1.50	1.90	0.8774
2nd best	1.00	1.25	1.90	0.8752
3rd	1.00	1.30	2.00	0.8644
4th	1.00	1.50	2.00	0.8611
5th	1.00	1.30	1.90	0.8504

Appendix C

All elemental X-ray maps that were obtained, but not included in the text, are presented here. The maps for each sample are preceded by an index image of the entire section, illustrating which grains were mapped.

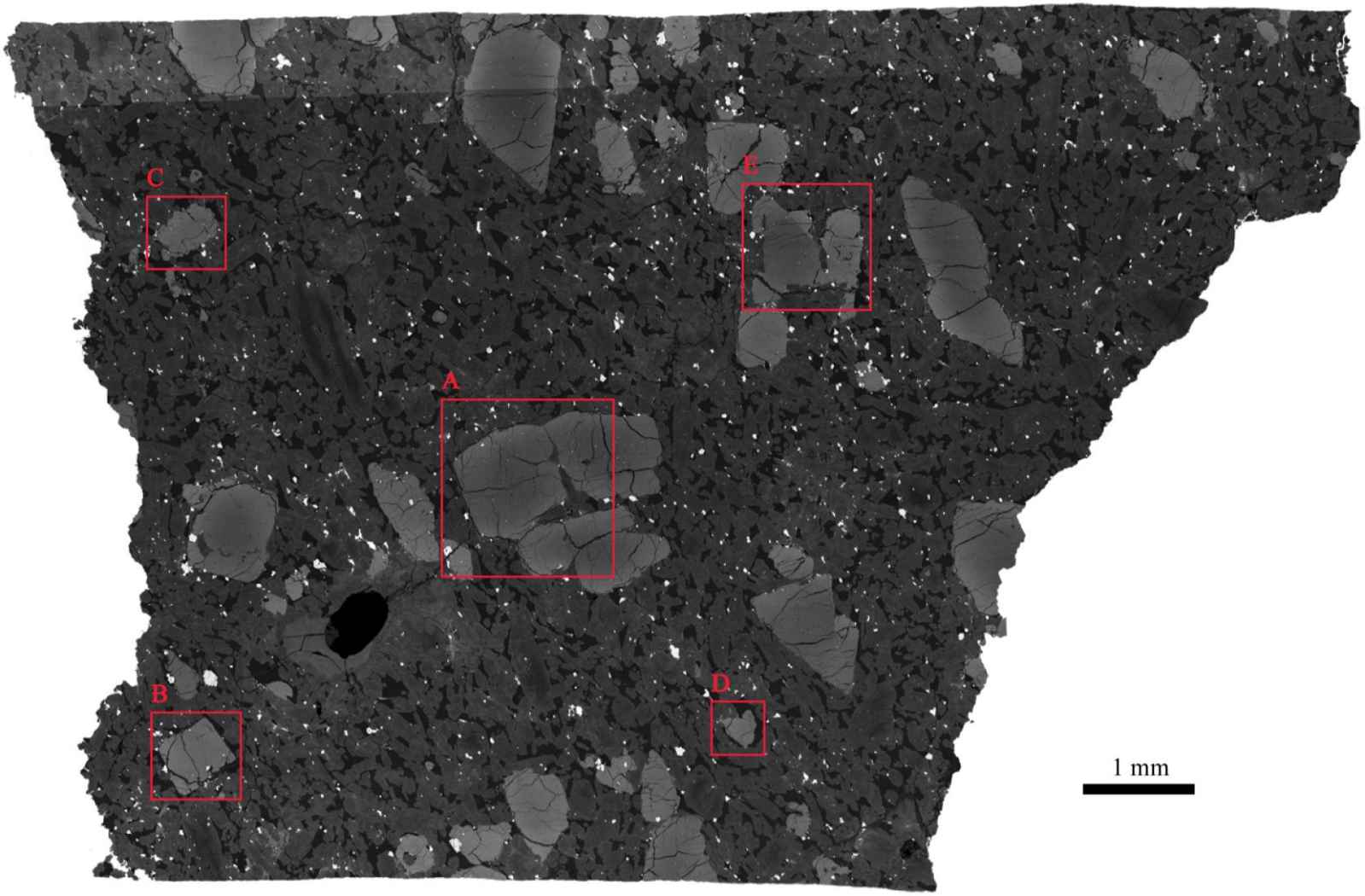

Figure 20. Elemental x-ray maps for olivine grains in DaG 476 were acquired for each of the areas outlined in red on the SEM image.

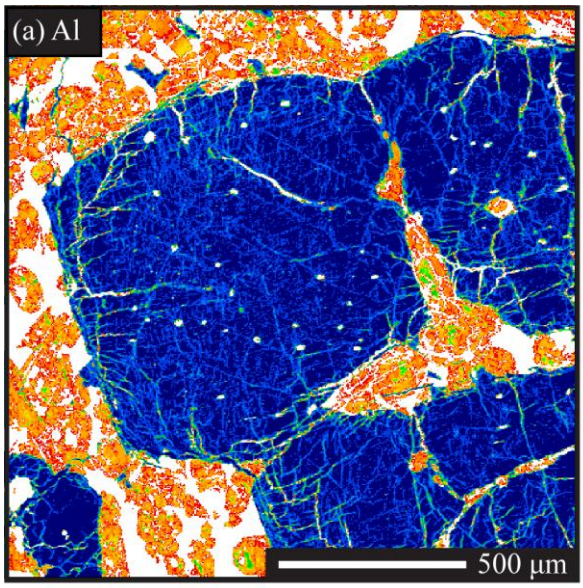

Figure 21. Al K_α x-ray map of DaG 476 olivine.

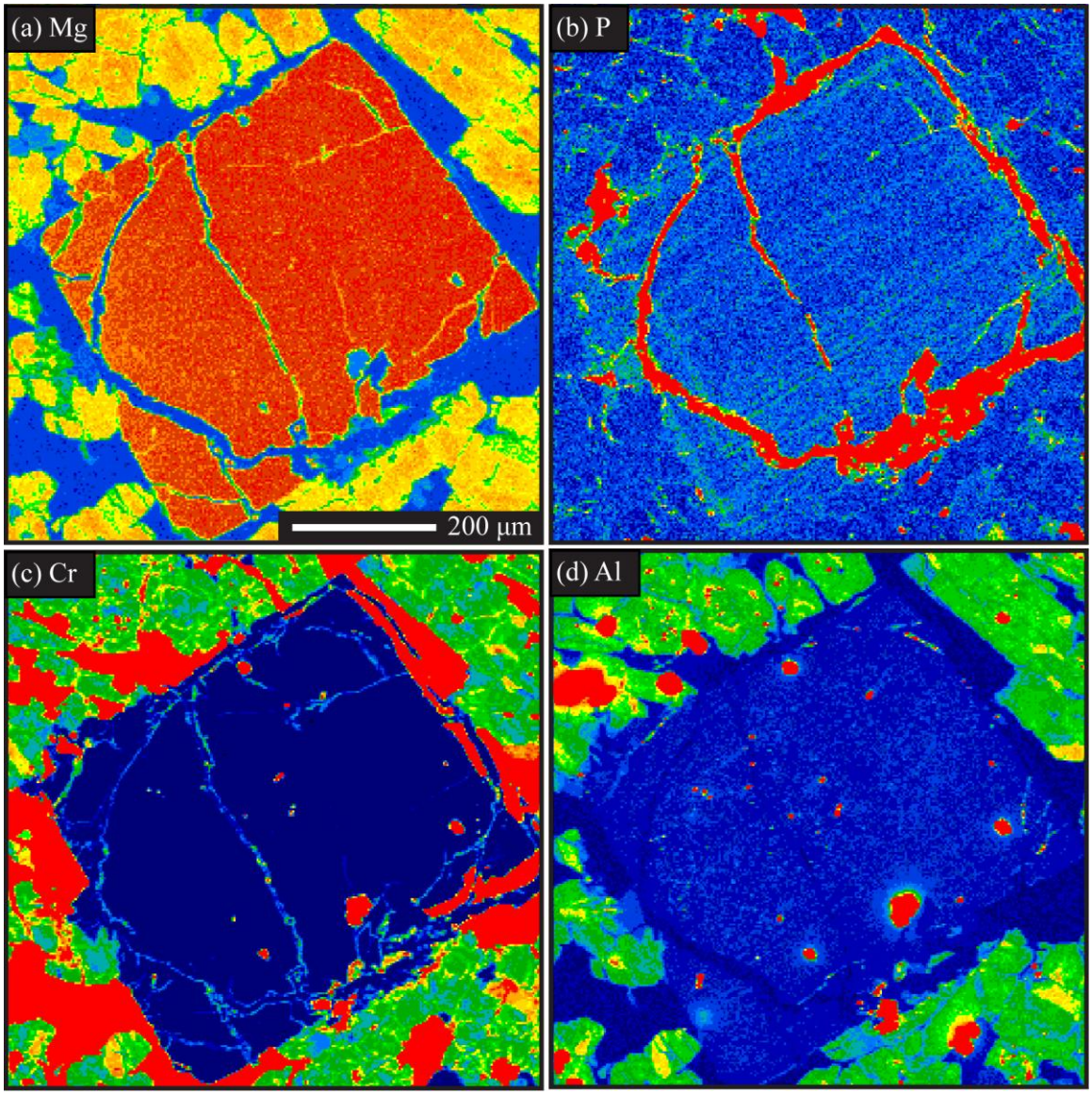

Figure 22. DaG 476 olivine grain. a) Mg K_β x-ray map. b) P K_α x-ray map. c) Cr K_α x-ray map. d) Al K_α x-ray map.

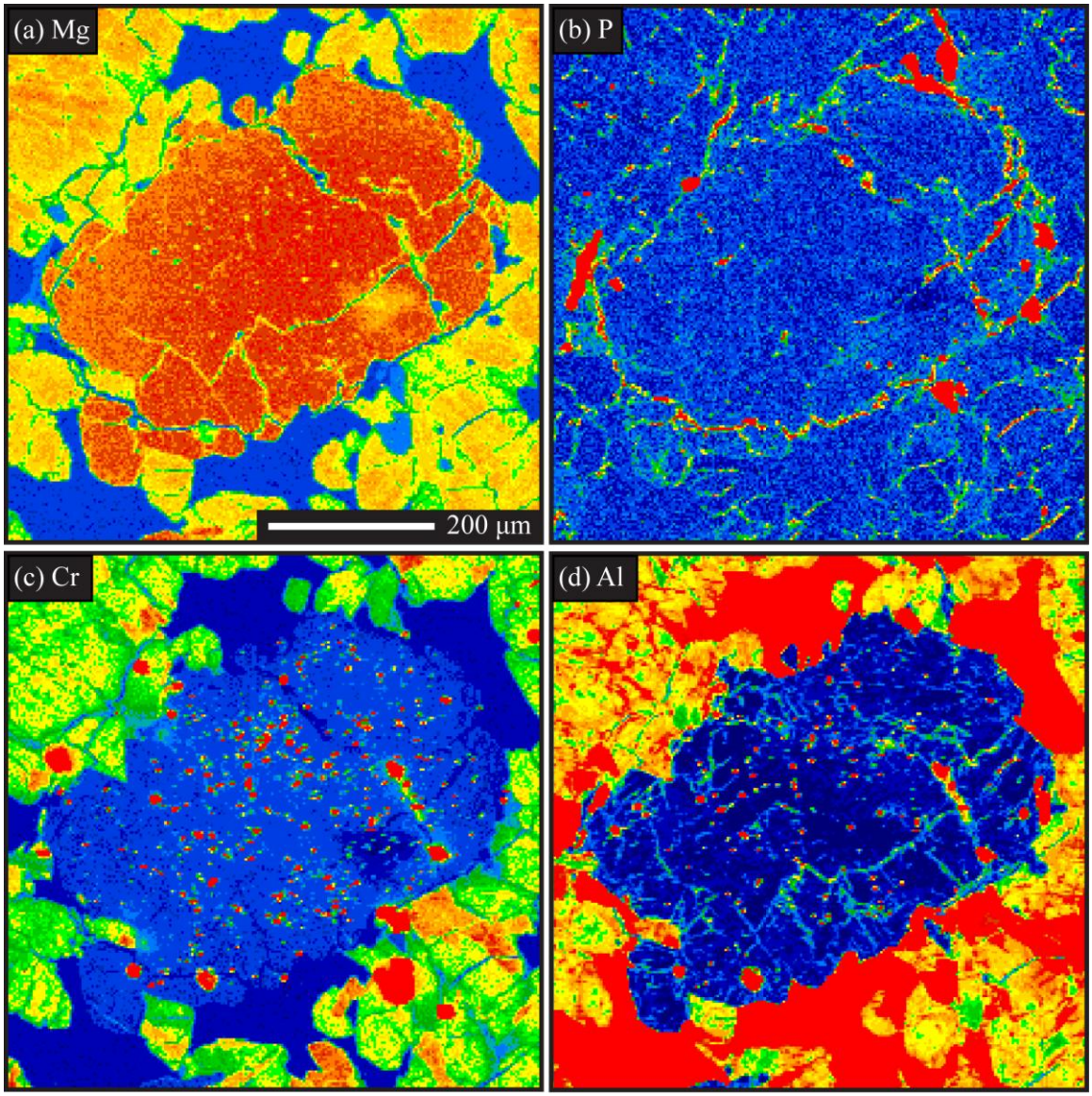

Figure 23. DaG 476 olivine grain. a) Mg K_β x-ray map. b) P K_α x-ray map. c) Cr K_α x-ray map. d) Al K_α x-ray map.

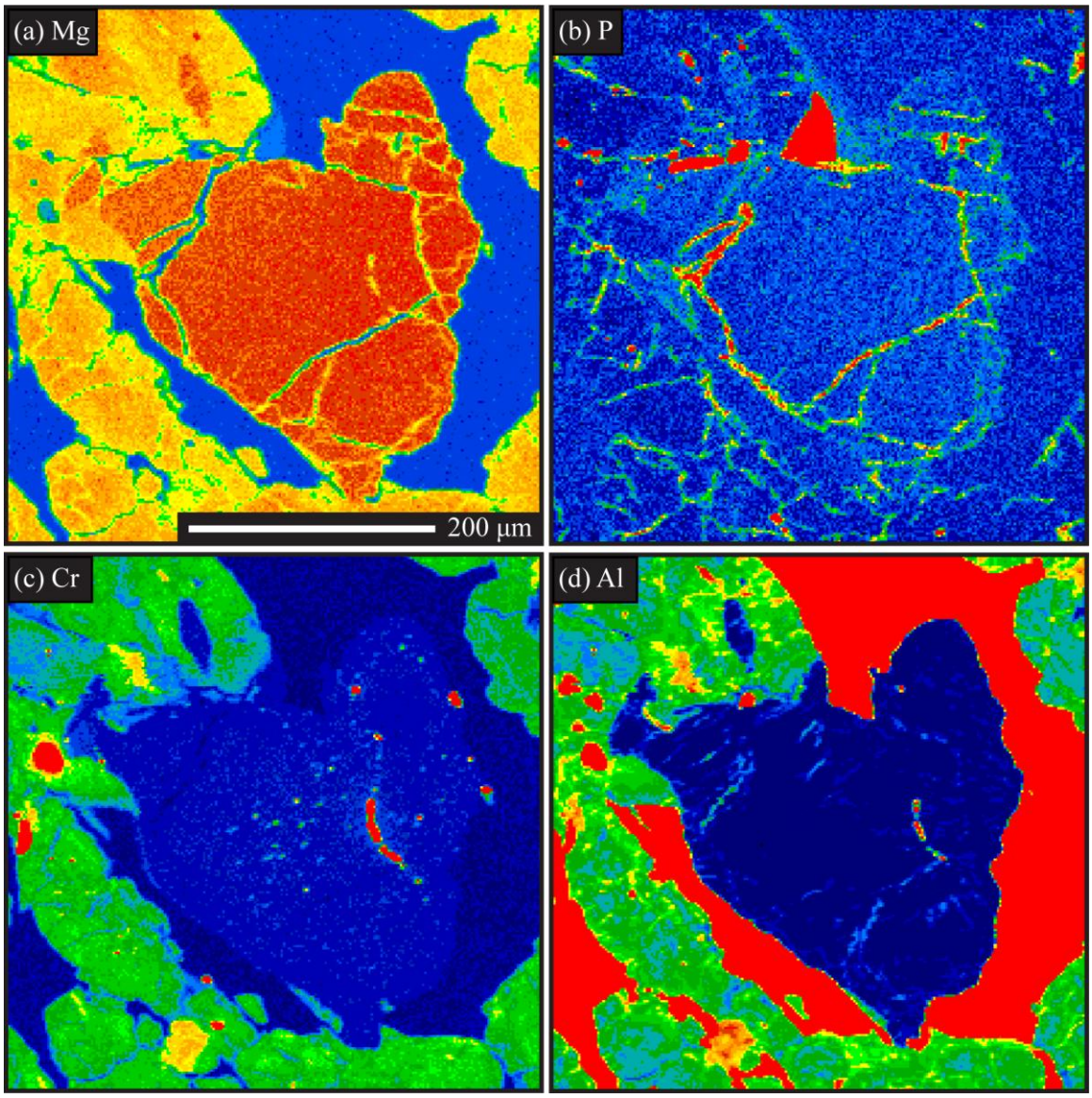

Figure 24. DaG 476 olivine grain. a) Mg K_β x-ray map. b) P K_α x-ray map. c) Cr K_α x-ray map. d) Al K_α x-ray map.

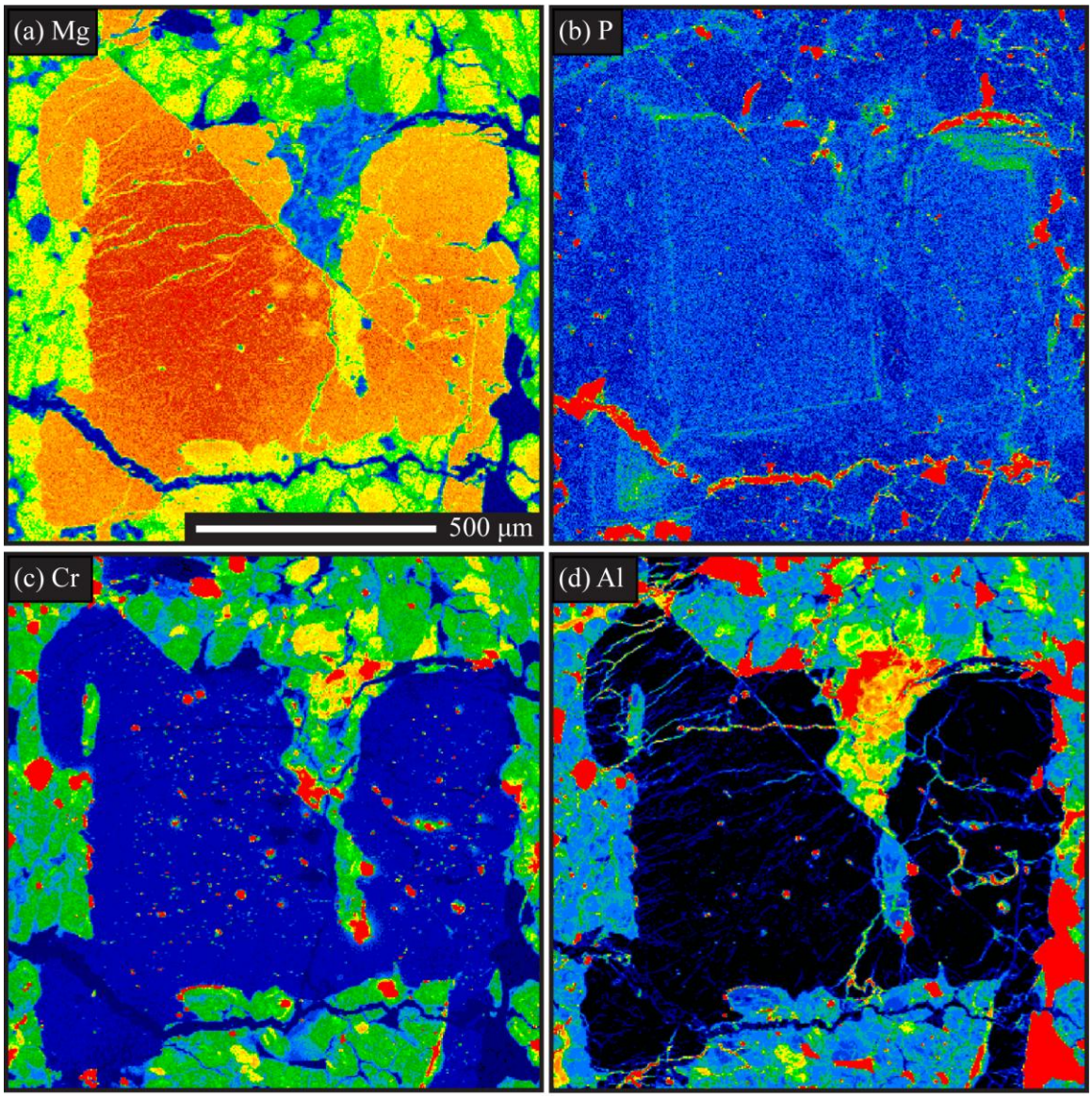

Figure 25. DaG 476 olivine grain. a) Mg K_β x-ray map. b) P K_α x-ray map. c) Cr K_α x-ray map. d) Al K_α x-ray map.

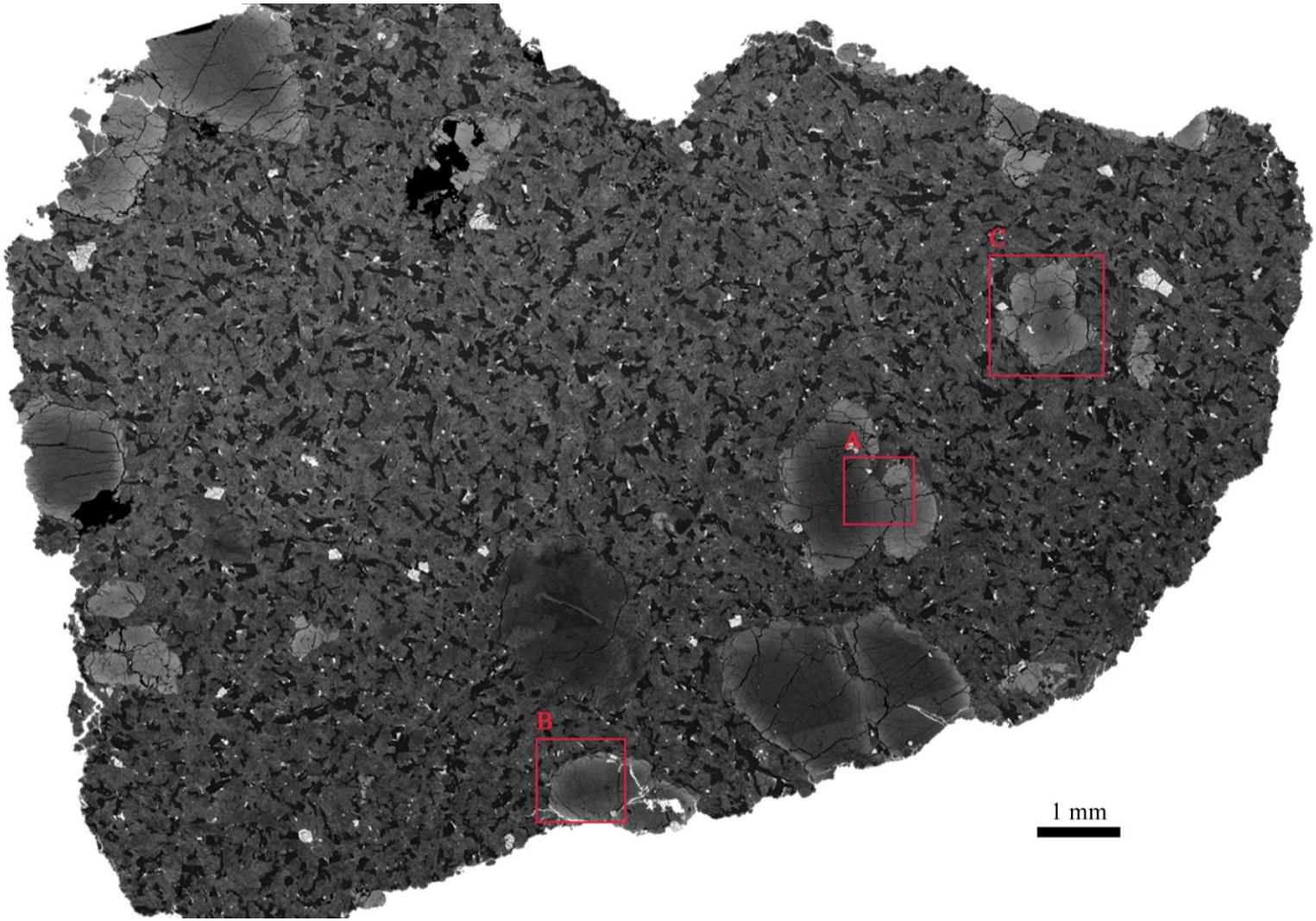

Figure 26. Elemental X-ray maps for olivine grains in EET 79001A were acquired for each of the areas outlined in red on the SEM image.

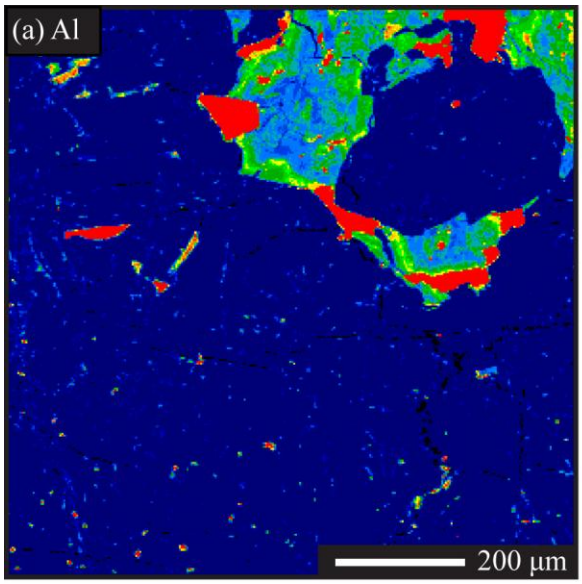

Figure 27. Al K_α x-ray map of EET 79001A olivine.

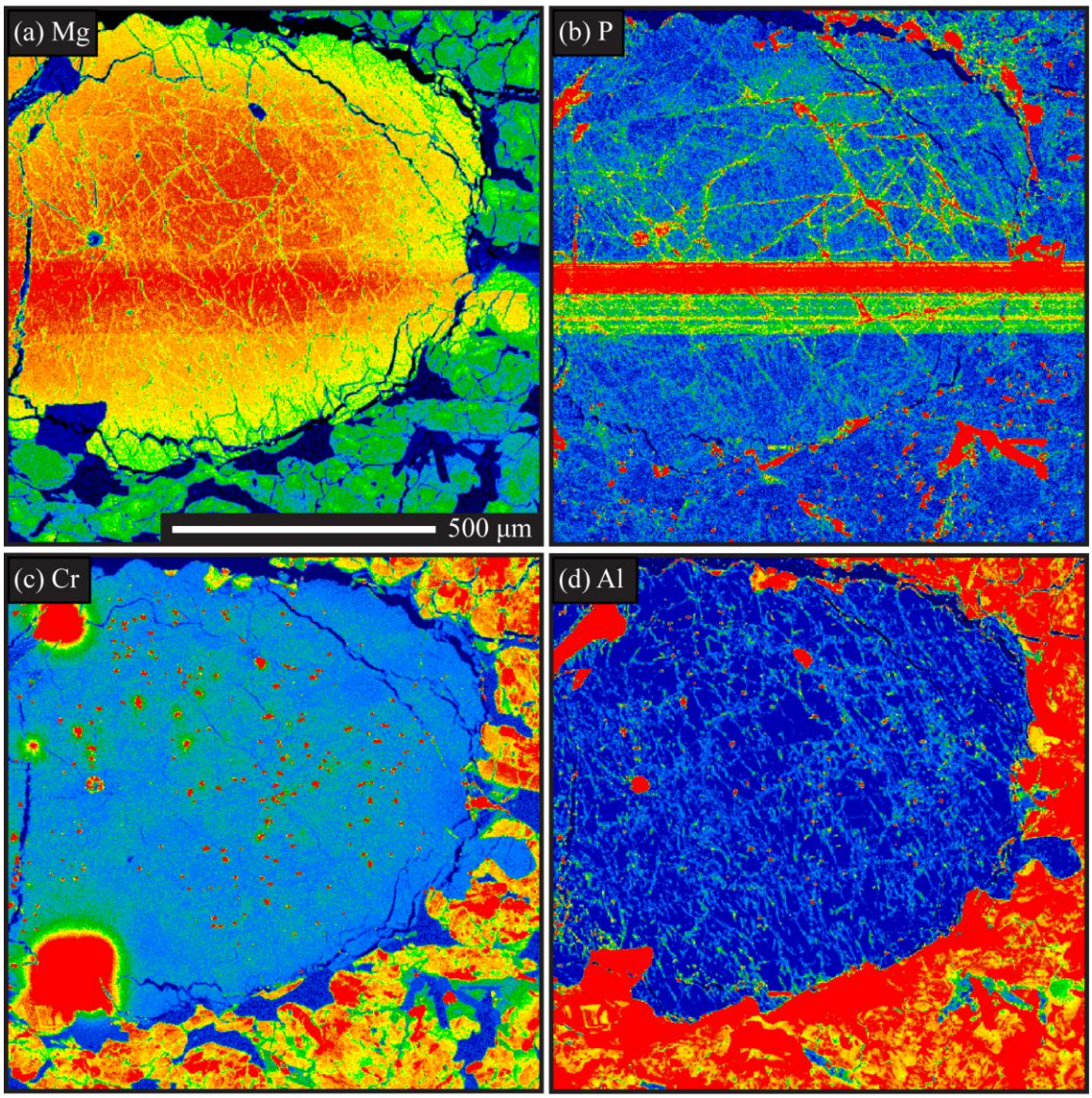

Figure 28. EET 79001A olivine grain. a) Mg K_β x-ray map. b) P K_α x-ray map. c) Cr K_α x-ray map. d) Al K_α x-ray map.

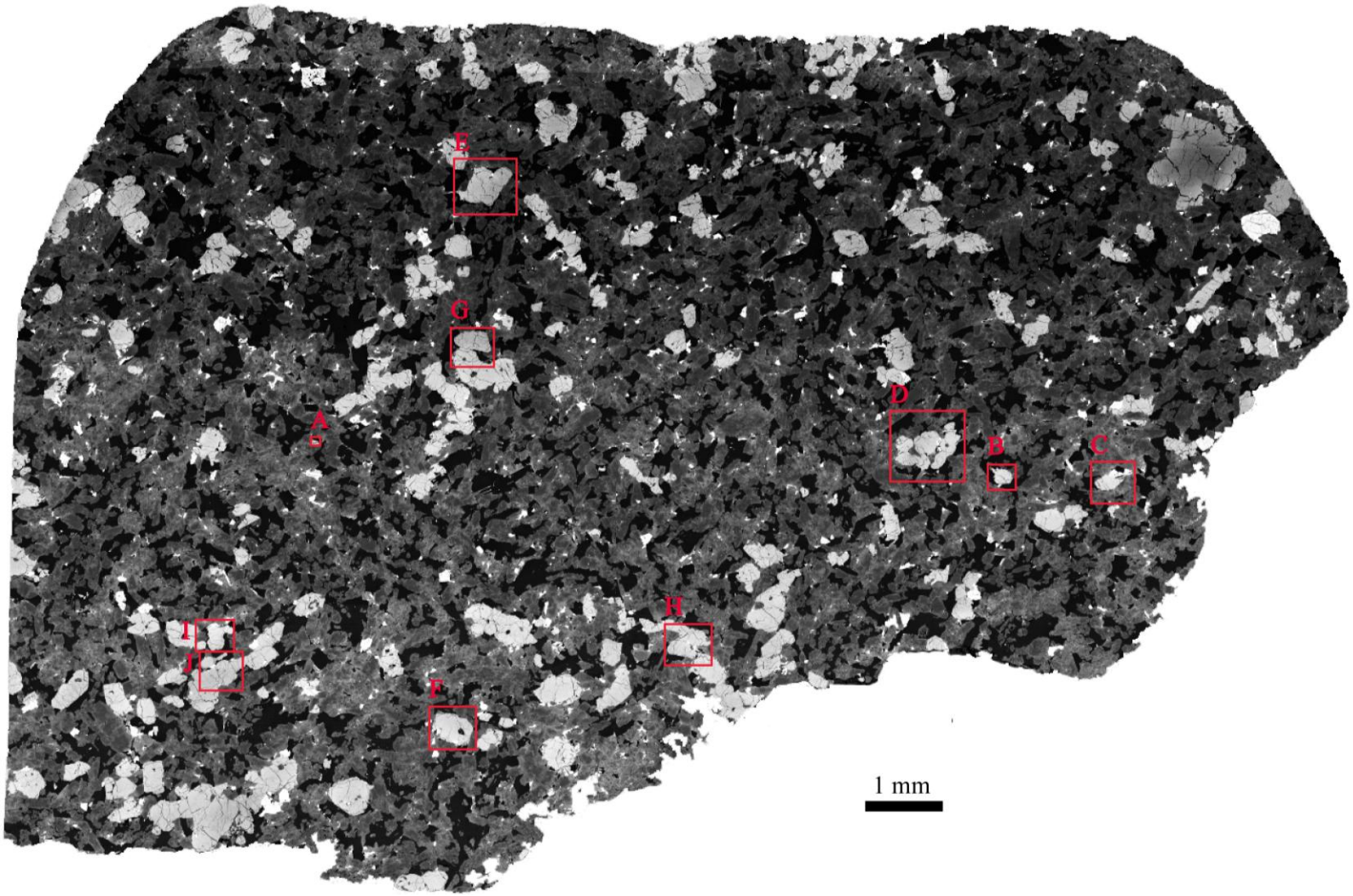

Figure 29. Elemental X-ray maps for olivine grains in Dho 019 were acquired for each of the areas outlined in red on the SEM image.

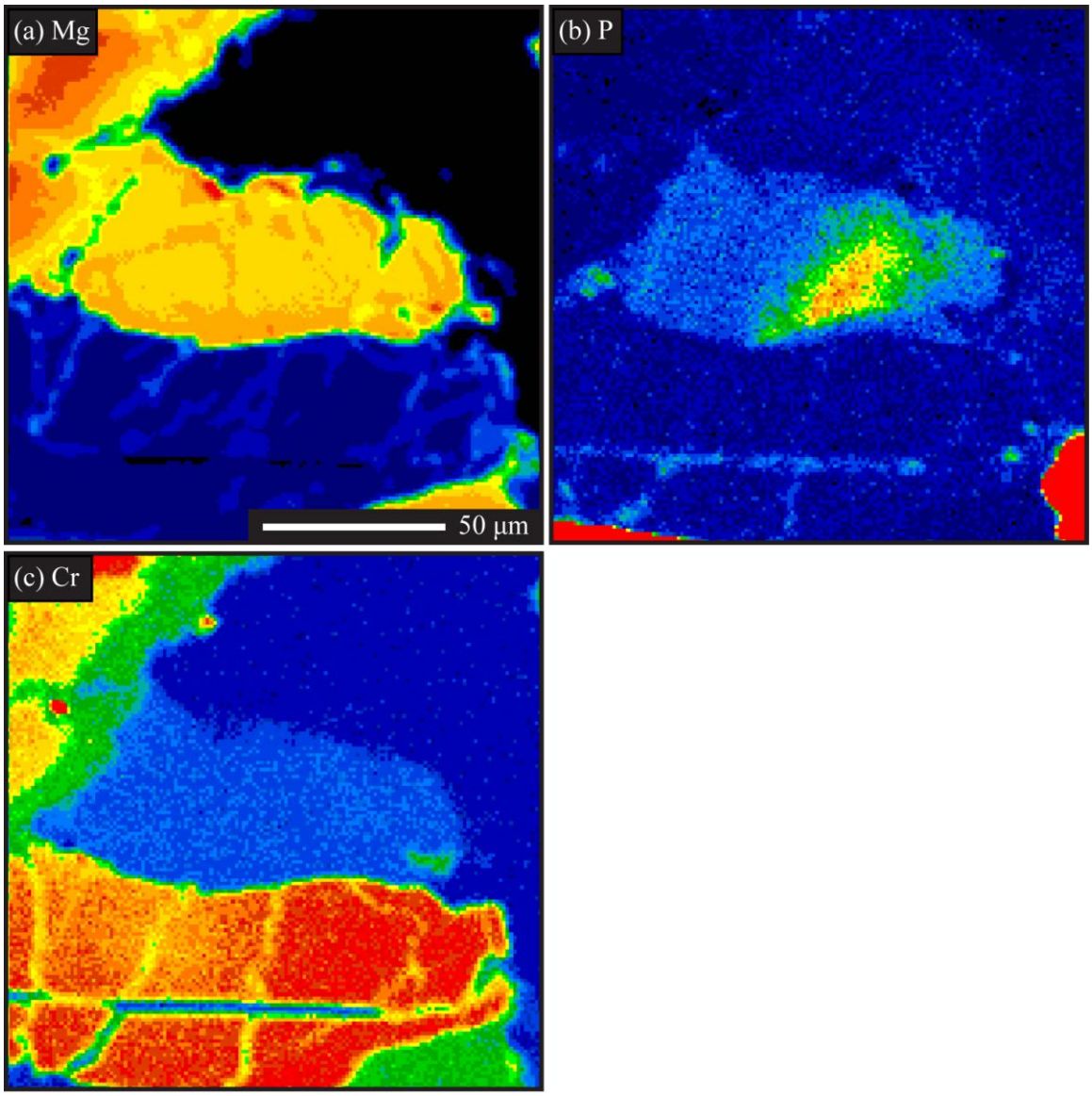

Figure 30. Dho 019 olivine grain. a) Mg K_β x-ray map. b) P K_α x-ray map. c) Cr K_α x-ray map.

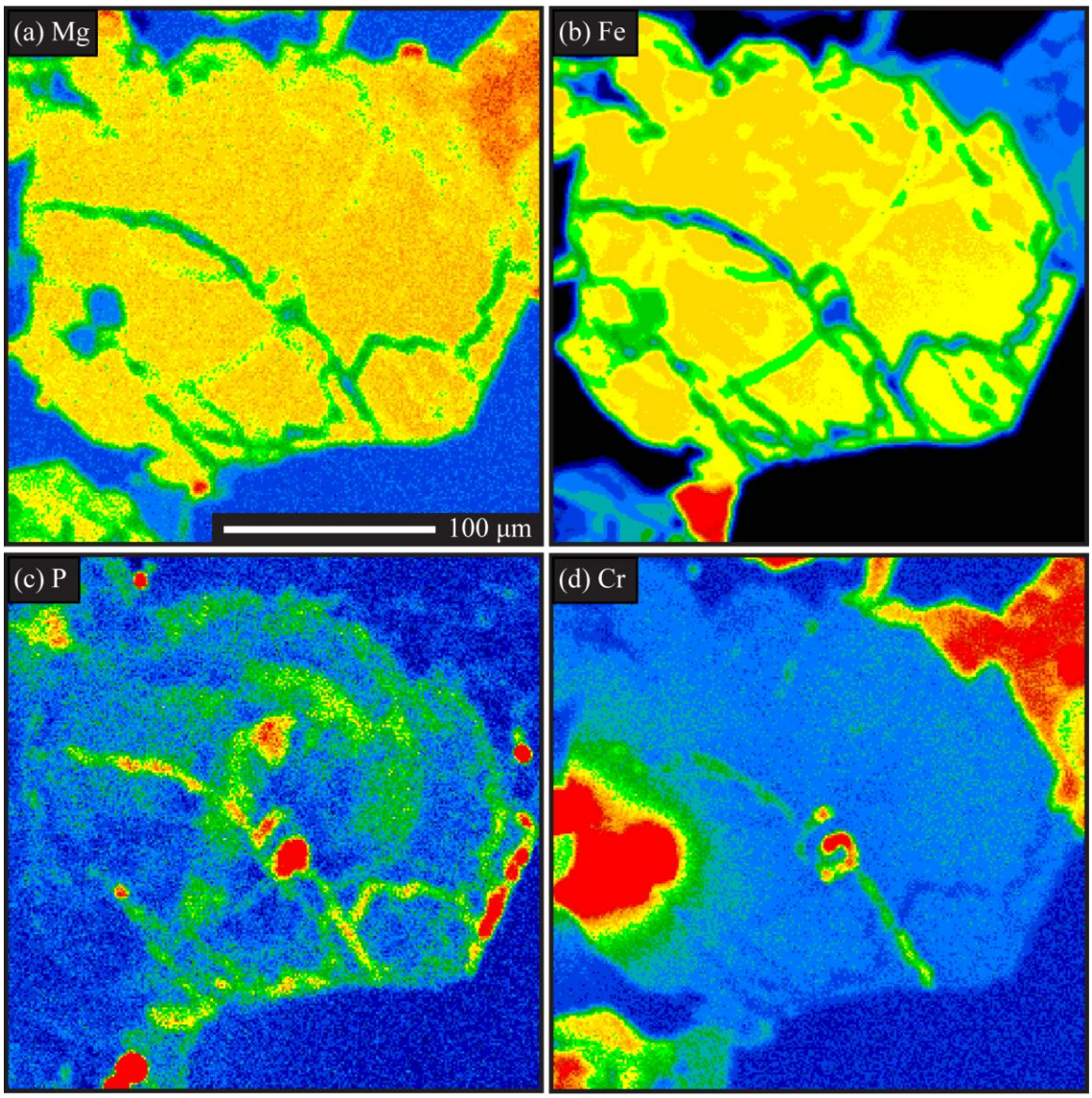

Figure 31. Dho 019 olivine grain. a) Mg K_β x-ray map. b) Fe K_α x-ray map. c) P K_α x-ray map. d) Cr K_α x-ray map.

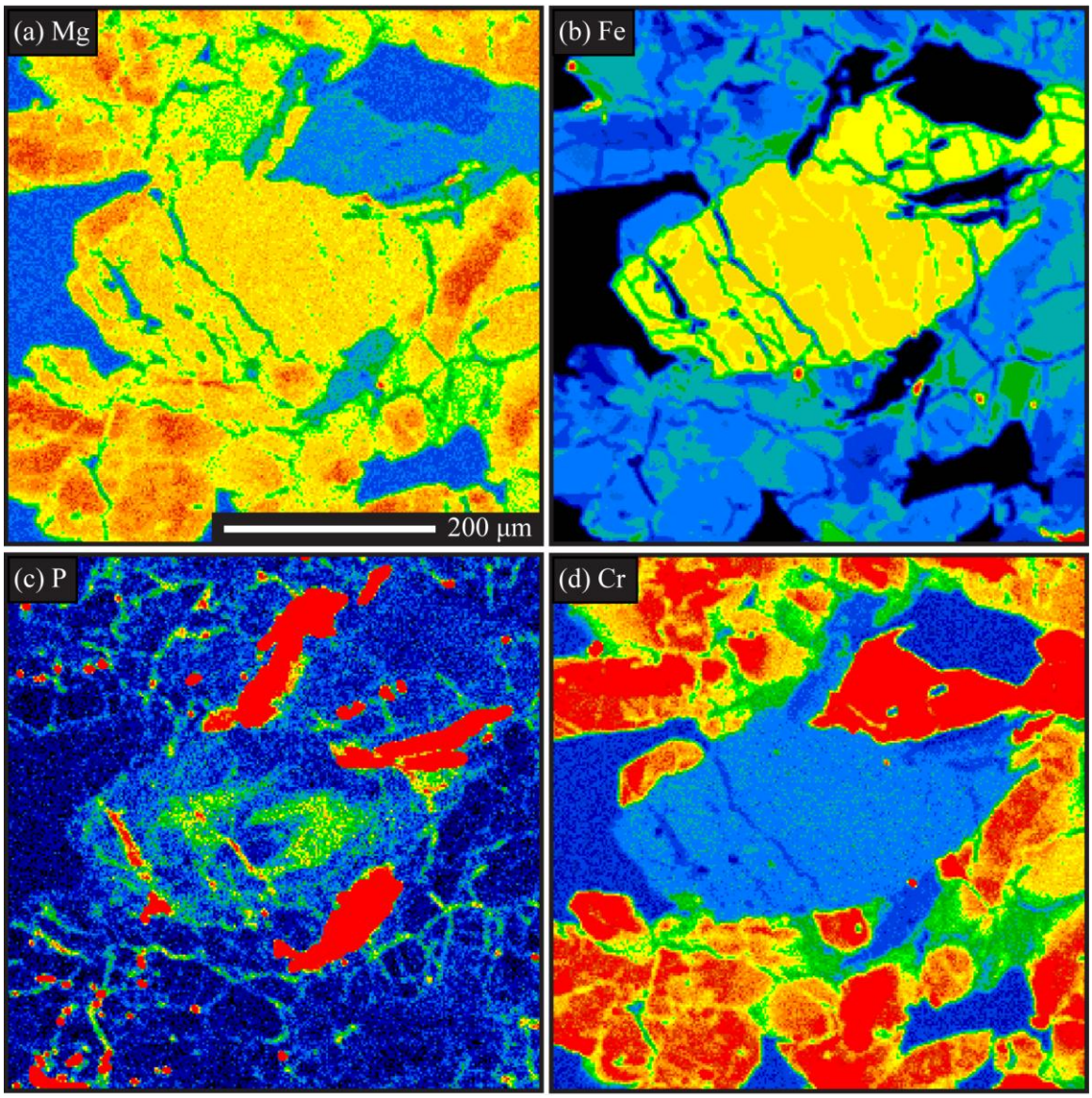

Figure 32. Dho 019 olivine grain. a) Mg K_β x-ray map. b) Fe K_α x-ray map. c) P K_α x-ray map. d) Cr K_α x-ray map.

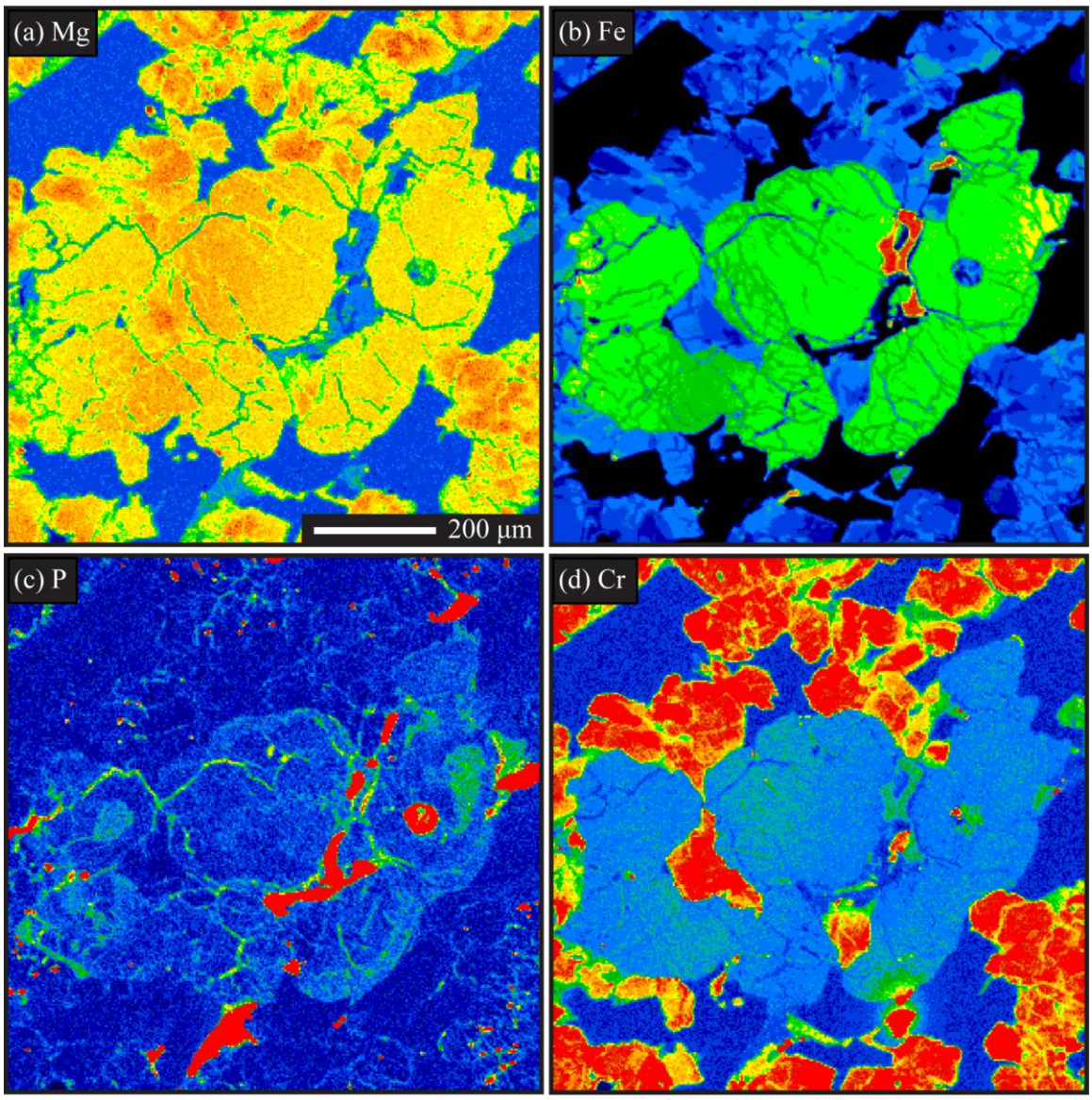

Figure 33. Dho 019 olivine grain. a) Mg K_β x-ray map. b) Fe K_α x-ray map. c) P K_α x-ray map. d) Cr K_α x-ray map.

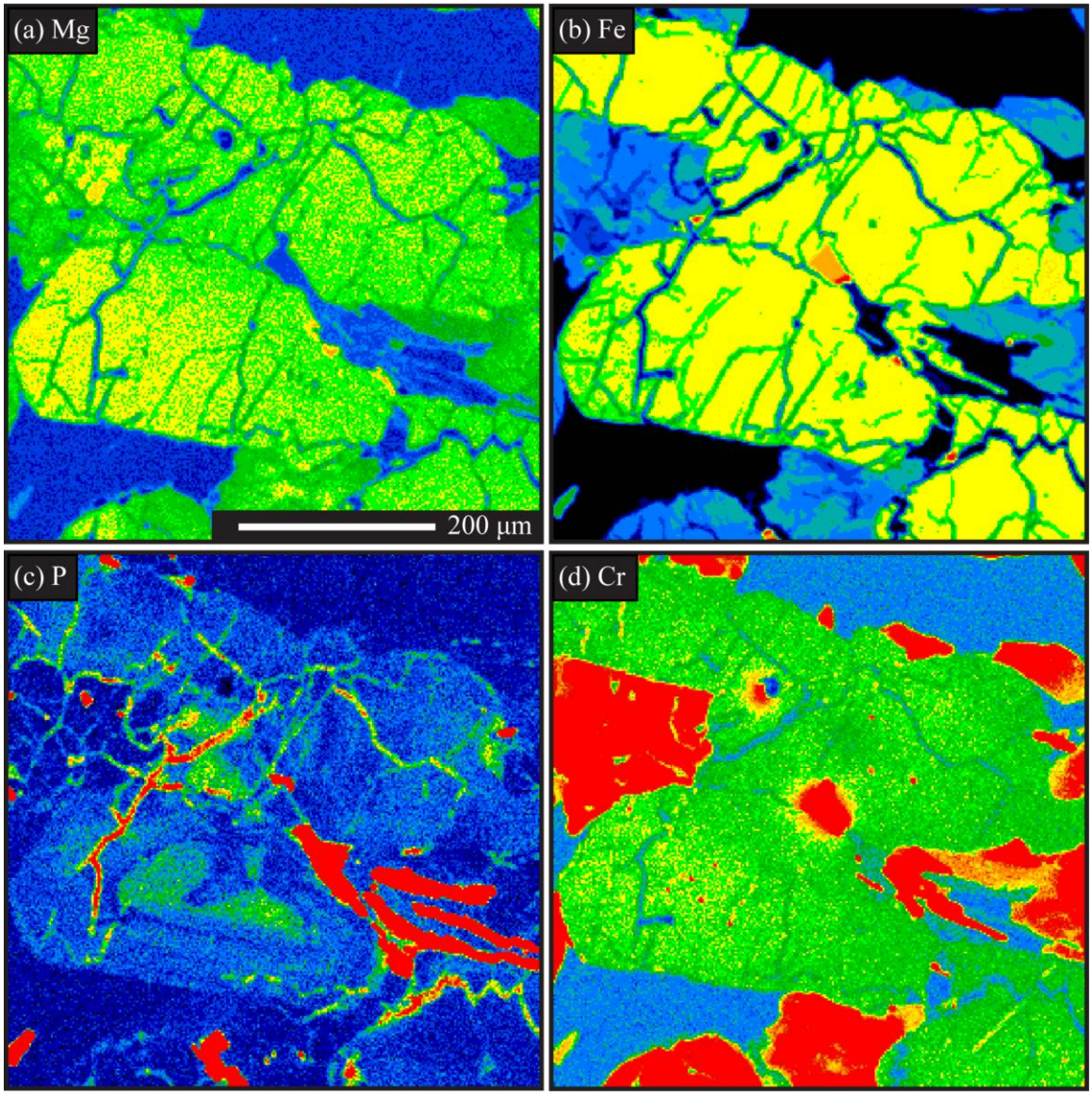

Figure 34. Dho 019 olivine grain. a) Mg K_β x-ray map. b) Fe K_α x-ray map. c) P K_α x-ray map. d) Cr K_α x-ray map.

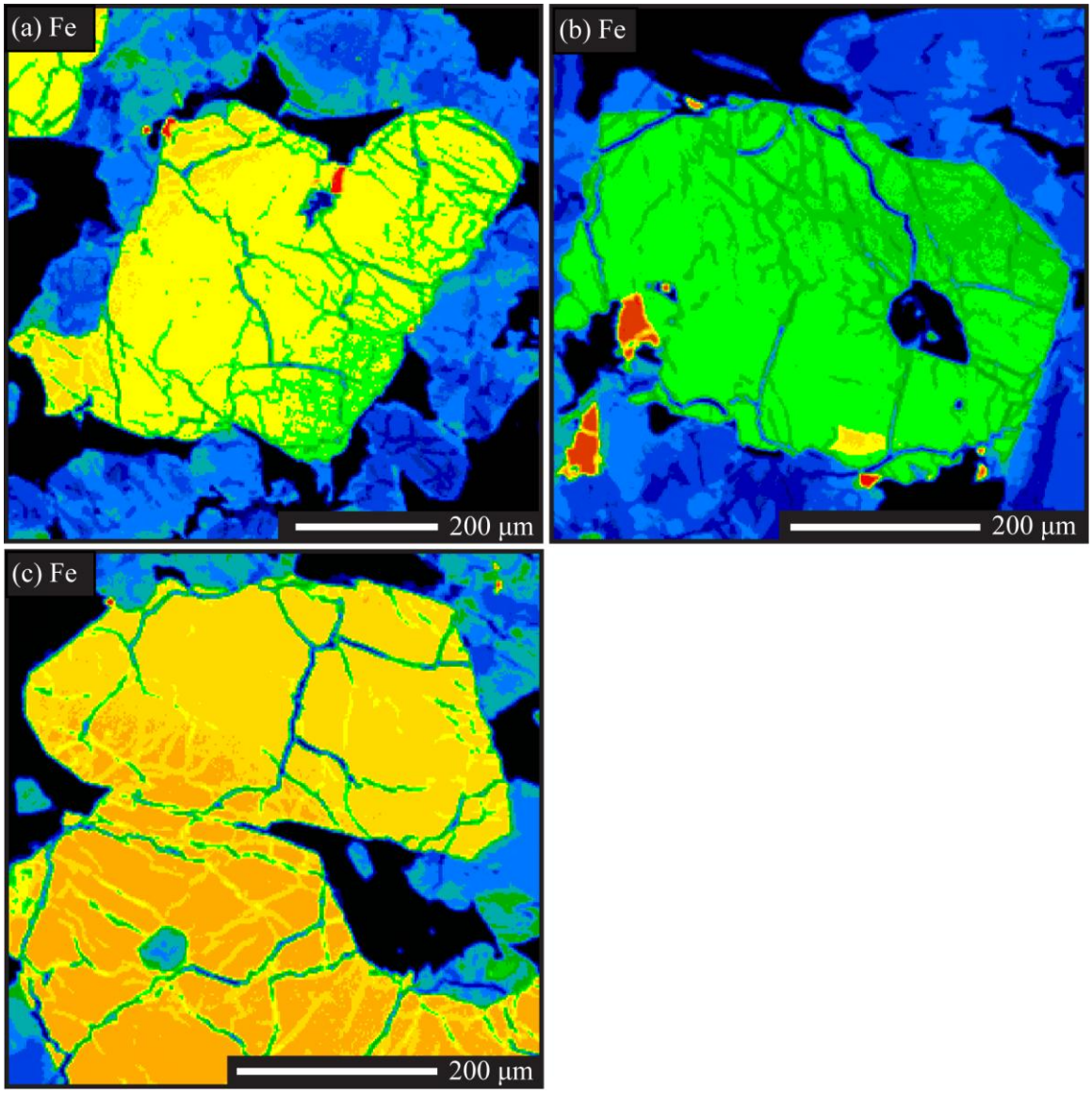

Figure 35. Fe K_α x-ray maps for olivines in a) figure 9, b) figure 5g-i, and c) figure 5j-l.

VITA

Megan Elizabeth Ennis was born on August 4th, 1983 in Allentown, Pennsylvania. She spent the early years of her life in Minnesota before the family settled in West Liberty, Kentucky where she attended Morgan County High School. Much time was spent outdoors, growing up in a small country town with an older brother and two younger sisters.

After graduating high school, Megan enrolled at Morehead State University, where she took full advantage of undergraduate research opportunities and summer internships at the Jet Propulsion Laboratory and the Smithsonian Natural History Museum. She graduated in August of 2008 with a Bachelor of Science in Geology and in Space Science.

In the fall of 2008, she entered into the Earth and Planetary Sciences graduate program at the University of Tennessee, Knoxville. While at UT she took courses in geology, chemistry and material sciences in pursuit of a Master of Science degree. She also taught undergraduate laboratory classes at UT, including Mineralogy and Introduction to Geology. In 2012, she was awarded a Master of Science in Teaching and taught 7th grade science for one year before completing her research, which is culminated in this document. She expects to be awarded her Master of Science degree in Geology in May 2014.